

1 **Title:** Length-dependent disassembly maintains four different flagellar lengths in *Giardia*

2

3 McInally SG¹, Kondev J², and Scott C. Dawson¹

4

5 Department of Microbiology and Molecular Genetics

6 One Shields Avenue

7 UC Davis

8 Davis, CA 95616

9

10 Department of Physics

11 Brandeis University

12 MS 057, 415 South Street,

13 Waltham, MA 02454

14

15

16 Corresponding author: scdawson@ucdavis.edu

17

18 **Running Title:** Flagellar length control in multiciliated *Giardia*

19 **Keywords:** *Giardia*, intraflagellar transport, multiciliated, length control

20

1 **Abstract**

2 How flagellar length regulation is achieved in multiciliated eukaryotic cells with flagella of
3 different equilibrium lengths is unknown. The protist *Giardia lamblia* is an ideal model to
4 evaluate length regulation as it has flagella of four different lengths. *Giardia* axonemes have
5 both non-membrane-bound and membrane-bound regions, but lack transition zones. Here we
6 quantified the contributions of intraflagellar transport (IFT)-mediated assembly and kinesin-13-
7 mediated disassembly to length control. IFT particles assemble and inject at *Giardia's* flagellar
8 pore complexes, which act as diffusion barriers functionally analogous to the transition zone to
9 compartmentalize the membrane-bound regions of flagella. IFT-mediated assembly is length-
10 independent as train size, speed, and injection frequencies are similar between flagella of
11 different lengths. In *Giardia*, kinesin-13 mediates a length-dependent disassembly mechanism
12 of length regulation to balance length-independent IFT-mediated assembly, resulting in
13 different lengths. We anticipate that similar control mechanisms are widespread in multiciliated
14 cells where cytoplasmic precursor pools are not limiting.

15

16

17

1 Introduction

2 Eukaryotic flagella and cilia (used interchangeably) are dynamic, membrane-bound and
3 compartmentalized microtubule-based organelles that facilitate diverse cellular behaviors
4 including motility, chemosensation, and directing hydrodynamic flow during development
5 (Brooks & Wallingford, 2014; Pazour & Witman, 2003). Composed of over 500 distinct proteins,
6 motile cilia are defined by the highly conserved axoneme structure consisting of nine
7 microtubule doublets surrounding a central pair of microtubules (“9+2”) (Ishikawa, 2017).
8 Axonemes are nucleated from mature centrioles or basal bodies, and extend from the complex
9 transition zone (TZ), which acts diffusion barrier or ‘gate’ at the base of cilia (Reiter, Blacque, &
10 Leroux, 2012). Due to its wide conservation in diverse microbial and multicellular flagellates,
11 eukaryotic flagellar architecture likely predates the radiation of all extant lineages (Ishikawa,
12 2017; Sung & Leroux, 2013). Yet eukaryotic morphological diversity is vast, and many
13 eukaryotes possess flagella with varied size, structure, and function presumably evolved from
14 conserved flagellar components and assembly mechanisms (Avidor-Reiss, Ha, & Basiri, 2017;
15 Ishikawa, 2017). Studies of flagellar assembly and length maintenance in diverse microbial
16 eukaryotic lineages allow us to address a central question in evolutionary cell biology: how does
17 cytoskeletal structural and functional variation arise from conserved cytoskeletal components
18 and mechanisms?

19 Foundational studies in the green alga *Chlamydomonas reinhardtii* showed that
20 axoneme assembly requires that the ciliary proteins synthesized in the cytoplasm are trafficked
21 to the growing distal tip of the axoneme through a bidirectional, microtubule motor-driven

1 process termed intraflagellar transport (IFT) (Kozminski, Johnson, Forscher, & Rosenbaum,
2 1993; Lechtreck, 2015). Assembly and maintenance of flagellar length is dependent upon IFT to
3 provide building blocks to the site of assembly, the distal flagellar tip (Kozminski et al., 1993;
4 Marshall & Rosenbaum, 1999). The components of IFT, including IFT particles, the BBsome,
5 kinesin and dynein motors, and transition zone (TZ) complex proteins are widely conserved in
6 free-living and parasitic unicellular flagellates such as *Tetrahymena*, *Leishmania*, *Trypanosoma*,
7 and in the ciliated cell types of *C. elegans* and mammals (Buisson et al., 2013; Hao et al., 2009;
8 Kozminski et al., 1993). Like variations in axoneme structure, variations in the IFT-mediated
9 ciliogenesis mechanisms are also present in many flagellated unicellular protists—notably, such
10 variations in axoneme number, structure, and assembly mechanism are hallmark features of
11 many metazoan cell types (Brooks & Wallingford, 2014; Ishikawa, 2017). Atypical axoneme
12 structure (e.g., primary cilia) can be the result of IFT-dependent mechanisms, and conversely
13 the canonical axoneme (9+2) structure can be assembled through alternative IFT-independent
14 “cytosolic ciliogenesis” mechanisms as described in apicomplexan parasites or in metazoan
15 sperm (Avidor-Reiss & Leroux, 2015). Lastly, many common eukaryotes possess from two to
16 thousands of cilia with diverse functions, lengths, morphologies, or inheritance patterns (e.g.,
17 the multiciliated protozoan *Tetrahymena* or multiciliated human epithelial cells). Is flagellar
18 structural diversity explained simply by the fact that some lineages have tinkered with ancient,
19 conserved IFT-mediated assembly and maintenance mechanisms, or have some flagellates
20 evolved alternative flagellar assembly mechanisms?

21 The unicellular, parasitic protist *Giardia lamblia* is an ideal model organism to address
22 the question of how unique flagellar types and flagellar lengths are built and maintained within

1 a single multiciliated cell. *Giardia* has eight flagella organized as four bilaterally symmetric pairs
2 with four different equilibrium lengths, implying a regulatory mechanism for sensing and
3 differentially modulating assembly or disassembly rates. Equilibrium axoneme lengths of all
4 eight flagella are also sensitive to microtubule stabilizing or depolymerizing drugs (Dawson et
5 al., 2007). While each of the eight *Giardia* axonemes maintains the characteristic ‘9+2’
6 microtubule architecture, each axoneme also has a cytoplasmic, non-membrane-bound region
7 that extends from a centrally located basal body before exiting the cell body as a membrane-
8 bound flagellum (McInally & Dawson, 2016). Homologs of IFT–BBSome transport proteins, and
9 kinesin-2 and dynein homologs are present in the genome, yet *Giardia* lacks a transition zone or
10 TZ protein homologs (Avidor-Reiss & Leroux, 2015; Barker, Renzaglia, Fry, & Dawe, 2014).
11 Lastly, during cell division and flagellar duplication, four intact mature axonemes and basal
12 bodies are structurally inherited and four new axonemes are assembled *de novo* in each
13 daughter cell (Hardin et al., 2017; Nohynková, Tumová, & Kulda, 2006). Cytoplasmic regions of
14 the *de novo* posteriolateral and ventral axonemes are rapidly assembled prior to cytokinesis
15 (Hardin et al., 2017).

16 The unique architecture and varied equilibrium lengths of *Giardia*’s eight flagella
17 challenge canonical models of IFT-mediated flagellar assembly and length regulation. Flagella
18 are classic models to study organelle size control, as each flagellum maintains a consistent
19 steady-state, or equilibrium length, and the size of flagella can be represented in a single
20 dimension, length (Marshall et al., 2005; Tamm, 1967). The prevailing explanation for
21 regulation of equilibrium flagellar length is the “balance-point model”, which argues that
22 constitutively controlled steady-state length is a balance between a length-dependent assembly

1 rate and a length-independent disassembly rate (Marshall et al., 2005). Equilibrium length can
2 be altered by modulating the rates of flagellar assembly or disassembly (Mohapatra, Goode,
3 Jelenkovic, Phillips, & Kondev, 2016). The classic “long-zero” experiment in *Chlamydomonas*
4 demonstrated length equalization of both flagella when one was amputated, defining the
5 paradigm for flagellar length control across diverse eukaryotic cells (Coyne & Rosenbaum,
6 1970). Yet how are the four pairs of flagella in *Giardia* with *different* equilibrium cytoplasmic
7 and membrane-bound flagellar lengths assembled and regulated in the same cell? Do
8 multiciliated cells with different lengths require alternative mechanisms to assemble, maintain,
9 and regulate distinct flagellar lengths?

10 To evaluate how *Giardia* differentially maintains and regulates different flagellar
11 lengths, we quantified the dynamics of both IFT-mediated assembly and kinesin-13 mediated
12 disassembly along the entire length of all axonemes – from the cytoplasmic basal bodies to the
13 membrane-bound tips. By tracking IFT particle behavior and turnover in live cells in
14 unprecedented detail, we discovered that the eight flagellar pore regions essentially act as the
15 diffusion barriers for each flagellar compartment. IFT particles diffuse bidirectionally on the
16 cytoplasmic regions and accumulate at each flagellar pore where IFT trains are assembled and
17 injected into the membrane-bound axonemes, rather than at basal body or transition zone
18 regions. We also determined that *Giardia* IFT train speed, size, and frequency of injection are
19 similar regardless of the length of the flagellar pair. Increasing flagellar lengths with the MT-
20 stabilizing drug Taxol also did not change the injection rate of IFT. *Giardia* kinesin-13 promotes
21 microtubule disassembly and turnover of tubulin subunits at distal flagellar tips (Dawson et al.,
22 2007), and here we show that kinesin-13 accumulates in a length-dependent manner to the

1 eight flagellar tips. Thus *Giardia* maintains four different equilibrium flagellar lengths by tuning
2 the rates of kinesin-13 mediated disassembly for specific flagellar pairs at the respective distal
3 tips. Lastly, we propose a new model for flagellar length regulation that emphasizes the length-
4 dependent disassembly process to balance a length-independent assembly rate for each
5 flagellar pair. We anticipate that the innovations in flagellar length regulation in *Giardia* will
6 echo known variations in flagellar structure, type, and number described in different human cell
7 types and other flagellated microbial model systems.

8

9 **Results**

10 ***Four different equilibrium lengths of cytoplasmic and membrane-bound axonemes***

11 The four flagellar pairs in *Giardia* have distinct lengths for both cytoplasmic and membrane-
12 bound regions of axonemes. The cytoplasmic axonemal regions span from the basal body to
13 flagellar pore (Figure 1A, shaded; 1B) and membrane-bound axonemal regions span from the
14 flagellar pore to flagellar tip (Figure 1A, colored). To quantify the average lengths and the range
15 of variation in lengths of both cytoplasmic and membrane-bound regions, we imaged
16 populations of fixed trophozoites expressing a single, integrated copy of mNeonGreen-tagged
17 β -tubulin to mark the MT cytoskeleton (Figure 1C). Total axoneme lengths (measured from
18 basal body to flagellar tip) vary between the four pairs. The anterior axonemes had an average
19 length of $19.1 \pm 0.4 \mu\text{m}$, the caudal flagella were $20.5 \pm 0.6 \mu\text{m}$, the posteriolateral flagella were
20 $16.2 \pm 0.4 \mu\text{m}$, and the ventral flagella were $16.8 \pm 0.9 \mu\text{m}$ (Supplemental Figure 1). We also
21 confirmed the average lengths of membrane-bound regions in WBC6 trophozoites: Anterior

1 flagella were $12.8 \pm 0.1 \mu\text{m}$, caudal flagella were $8.7 \pm 0.2 \mu\text{m}$, posteriolateral flagella were
2 $8.1 \pm 0.1 \mu\text{m}$, and ventral flagella were $13.7 \pm 0.9 \mu\text{m}$ (Figure 1D and (Hoeng et al., 2008)).

3

4 ***All IFT homologs localize to both cytoplasmic and membrane-bound regions of the all flagella***

5 IFT-mediated assembly of flagella requires the organization of IFT-A and IFT-B particles, kinesin
6 and dynein motors, and the BBSome into multi-megadalton complexes called IFT trains (Figure
7 1B and (Lechtreck, 2015)). While length maintenance of the membrane-bound regions of
8 *Giardia's* eight flagella is dependent on intraflagellar transport (IFT), the cytoplasmic regions are
9 hypothesized to be assembled by an IFT-independent mechanism (Dawson et al., 2007; Hoeng
10 et al., 2008). Previously, components of IFT-A (IFT140) and IFT-B (IFT81) were localized to both
11 the cytoplasmic and membrane-bound axonemal regions (Hoeng et al., 2008). To confirm and
12 extend this prior work, we imaged fluorescently tagged C-terminal fusions of all homologs of IFT
13 particles (12), BBSome components (3), and kinesin-2 motor proteins (2). All *Giardia* IFT-A
14 (IFT121, IFT122, IFT140) or IFT-B (IFT38, IFT54, IFT56, IFT57, IFT74/72, IFT80, IFT81, IFT88, and
15 IFT172) particle homologs localized to the eight basal bodies, flagellar pores, flagellar tips, and
16 along the lengths of both the cytoplasmic and membrane-bound regions of all axonemes
17 (Figure 2A and (Hoeng et al., 2008)). Anterograde kinesin-2a and kinesin-2b motors localized to
18 the eight flagellar pores and flagellar tips but had minimal localization to the cytoplasmic
19 axonemes or basal bodies (Figure 2A and (Hoeng et al., 2008)). Furthermore, the localization
20 puncta of IFT or kinesin-2 homologs at the flagellar tips are consistent with other studies of
21 kinesin-2 distribution in the flagellum (Chien et al., 2017; Hendel, Thomson, & Marshall, 2018).

1 Of the three BBSome homologs in *Giardia*, BBS4 localized primarily to the flagellar pores, BBS5
2 localizes primarily to the cytoplasmic axonemes, and BBS2 had cytoplasmic localization (Figure
3 2A). While distinct puncta of IFT trains were not observed on any of the cytoplasmic axonemes,
4 all IFT proteins densely localized to cytoplasmic regions of all eight axonemes.

5 To determine whether overexpression of IFT proteins from episomal plasmids prevents
6 observation of discrete IFT trains on the cytoplasmic axonemes, we also integrated
7 mNeonGreen-tagged IFT81 (IFT81mNG) or GFP-tagged IFT81 (IFT81GFP) into the native *Giardia*
8 IFT81 locus (Gourguechon & Cande, 2011) (Supplemental Figure 2). Strains expressing IFT81GFP
9 or IFT81mNG from an integrated copy of the gene had the same subcellular localization as
10 strains expressing tagged IFT81 from the episomal vector, but the labeling intensity was more
11 uniform in the population of transformants. IFT81mNG was at least 3-fold brighter than
12 IFT81GFP (Supplemental Figure 3).

13

14 ***Axoneme specific accumulation of IFT particles at different flagellar pores***

15 Due to the physical decoupling of the basal bodies and the membrane-bound regions of flagella
16 in *Giardia*, the location of IFT train assembly and injection has remained unclear (Avidor-Reiss &
17 Leroux, 2015). To determine the spatial distribution of IFT81mNG particles along the entire
18 lengths of axonemes (basal body to flagellar tip), we traced fluorescence with line scans in two
19 representative axonemal pairs (anterior and posteriolateral) in the IFT81mNG strain (Figure 2B).
20 IFT81mNG fluorescence was not uniformly distributed along the lengths of either the anterior
21 or posteriolateral axonemes (Figure 2B). The maximum fluorescence intensity for both flagellar

1 pairs occurred at the flagellar pore, a region that lies at the transition from the cytoplasm to the
2 compartmentalized flagellum (Figure 2C). IFT81mNG fluorescence in the anterior flagella had a
3 single distinct maximum at the flagellar pore, whereas the posteriolateral flagella had one
4 maximum at the posteriolateral flagellar pore and another maximum at a region immediately
5 proximal to the ventral flagellar pores (Figure 2C). IFT81 localized less to the basal bodies of the
6 anterior and posteriolateral axonemes than to the rest of the axoneme, in contrast to other
7 flagellates (Hao et al., 2011; Prevo, Mangeol, Oswald, Scholey, & Peterman, 2015). The
8 cytoplasmic regions of both the anterior and posteriolateral axonemes had higher intensities of
9 IFT81mNG fluorescence than the membrane-bound regions, albeit less intensity than at
10 flagellar pores. For all imaging experiments there was no difference in the localization of
11 IFT81mNG fluorescence between either axoneme of each flagella pair. Our analyses of
12 cytoplasmic axonemes were limited to the anterior and posteriolateral axonemes, as we were
13 unable to reliably measure fluorescence intensity from the cytoplasmic regions of caudal and
14 ventral flagella.

15

16 ***The diffusive behavior of IFT particles in cytoplasmic regions results in IFT train assembly at***
17 ***each flagellar pore region***

18 To understand how IFT particles accumulate in the flagellar pore regions in *Giardia*, we
19 interrogated the behavior and turnover of IFT particles associated with the cytoplasmic
20 axoneme and flagellar pore regions. Specifically, we used fluorescence recovery after
21 photobleaching (FRAP) in the IFT81mNG strain to determine whether IFT particles on

1 cytoplasmic axonemes are dynamic. After photobleaching the cytoplasmic regions of
2 posteriolateral flagella (Figure 3A, 3C, Supplemental Video 1), we determined that IFT particles
3 are dynamic on cytoplasmic axonemes and that recovery was also bi-directional. This analysis of
4 turnover indicates that fluorescently labeled IFT81 molecules likely traverse the cytoplasmic
5 axonemes in both anterograde and retrograde directions, despite our inability to detect distinct
6 IFT trains traversing these structures using live imaging (Figure 3A). To assess the contribution
7 of cytoplasmic axonemal IFT dynamics to the accumulation of IFT particles at each flagellar
8 pore, we used FRAP to evaluate the turnover of IFT particles in the flagellar pores of
9 posteriolateral axonemes (Figure 3B, 3D, Supplemental Video 2). IFT turnover was
10 approximately three times faster at the flagellar pore ($0.055 \pm 0.018 \mu\text{m s}^{-1}$) than in the
11 cytoplasmic region ($0.019 \pm 0.005 \mu\text{m s}^{-1}$) (Figure 3C, 3E).

12 Differences in the rates of IFT particle turnover between the cytoplasmic and
13 membrane-bound regions supports the idea that two processes promote the accumulation of
14 IFT at the flagellar pore: (1) diffusion of IFT particles from the cytoplasmic axoneme region and
15 (2) the return of IFT trains during retrograde transport (Figure 3F). To test this hypothesis, we
16 developed a physical model that compares the relative contribution of these two processes to
17 the accumulation of IFT particles at the flagellar pore. The model predicts a 3 ± 1 -fold difference
18 in the initial linear-phase of the recovery between flagellar pore and cytoplasmic axoneme
19 regions (Methods). We measured the slope of the initial linear-phase of recovery for these two
20 regions and found 4.2 ± 0.5 -fold difference (Figure 3C, 3D). Therefore, our model provides
21 additional support for the accumulation of IFT particles at flagellar pores due to the mixing of
22 IFT particles diffusing from the cytoplasmic regions with IFT particles returning via retrograde

1 transport from the membrane-bound axonemes (Figure 3F). The accumulation of IFT intensity
2 combined with the absence of directed IFT transport from the cytoplasmic regions is also
3 consistent with IFT train assembly occurring at each flagellar pore.

4

5 ***IFT particle size, frequency and speed are similar between flagellar pairs of differing lengths***

6 The balance point model of flagellar length control requires length-dependence of either the
7 assembly rate, the disassembly rate, or both rates to establish an equilibrium length. Thus the
8 maintenance of four different equilibrium flagellar lengths in *Giardia* could be due to either
9 differential rates of IFT-mediated assembly or disassembly (Mohapatra et al., 2016). To
10 evaluate length-dependent IFT-mediated assembly, we quantified and compared IFT dynamics
11 within the membrane-bound compartment of three of the four flagellar pairs, each with
12 different equilibrium lengths. We were unable to analyze IFT on the ventral flagella, which
13 continued to beat while embedded (Figure 4A, Supplemental Video 3). Anterograde (Figure 4B,
14 magenta) and retrograde (Figure 4B, green) IFT dynamics were compared using kymographs of
15 the anterior, posteriolateral, and caudal flagella pairs (Figure 4B). For each flagellar pair, we
16 quantified and compared the parameters of speed, size, and frequency of IFT trains undergoing
17 transport within the membrane-bound flagellar compartment (Figure 4C-4F)(Engel, Ludington,
18 & Marshall, 2009; Mangeol, Prevo, & Peterman, 2016).

19 For all flagella, the average IFT train speed was consistent for both anterograde and
20 retrograde directions, and IFT train speeds were not different between pairs of different
21 lengths. Specifically, the average anterograde IFT train speed for all flagellar pairs was between

1 3.0 - 3.2 $\mu\text{m}/\text{sec}$, with no significant differences between any of the measured flagella (Figure
2 4D). For all measured flagella, the retrograde IFT velocities were slightly greater than
3 anterograde velocities, which is consistent with IFT velocities in other flagellates (Buisson et al.,
4 2013). The average retrograde IFT velocity ($\sim 3.2 \mu\text{m}/\text{sec}$) was not significantly different
5 between any of the measured flagellar pairs (Figure 4E).

6 In contrast, there were notable differences in the size of IFT trains between the flagellar
7 pairs of different lengths, which could imply a length dependence of particle size for the
8 anterior and caudal flagellar pairs. The average size of anterograde particles in anterior flagella
9 was 24% larger than those in the shorter caudal flagella (Figure 4C). Retrograde IFT trains were
10 also 21% larger in the anterior as compared to the caudal flagella (Figure 4E). Anterior
11 anterograde or retrograde flagella IFT trains were also 11% larger as compared to the
12 posteriolateral flagella (Figure 4D, F) yet this difference is not statistically significant.

13 Comparisons of anterograde IFT injection frequency between anterior, caudal, and
14 posteriolateral flagella showed that IFT train injection is not significantly different between
15 flagellar pairs of different lengths (Figure 4C, 4D). Retrograde IFT frequency was also not
16 significantly different between flagellar pair of different lengths (Figure 4E, 4F). To compare and
17 confirm IFT injection frequency rates (trains/sec) between different pairs, we also measured
18 the time between each injection from kymographs filtered for only anterograde traffic (Figure
19 4B, magenta). The distribution of time-lag between injections is exponential, indicating a single
20 rate limiting step for IFT train injection in the anterograde direction for the three pairs analyzed
21 (Figure 4G). The frequency distribution was converted to a probability density function and a
22 single exponential fit was used to measure the rate of injection (Methods, and Figure 4G).

1 Overall, the frequency of anterograde IFT train injection was not significantly different between
2 longer (anterior) and shorter (caudal, posteriolateral) flagellar pairs. The average time between
3 IFT train injections was similar between the three flagellar pairs: 1.0 ± 0.1 seconds for the
4 anterior flagella; 1.3 ± 0.2 seconds for caudal flagella; and 1.2 ± 0.1 seconds for posteriolateral
5 flagella (Figure 4G).

6 ***Perturbation of flagellar length supports length independence of IFT injection***

7 Next, we queried whether the total number of IFT trains within each flagellar pair scales linearly
8 with length which is predicted by length-dependent IFT injection. For this analysis, we used 3D
9 structured illumination microscopy (3D-SIM) to quantify the total integrated intensity of IFT
10 trains in fixed trophozoites expressing integrated IFT81:GFP (Figure 5A) to provide an additional
11 line of evidence for these observations. Fluorescence intensity of IFT81GFP and length of the
12 membrane-bound regions of flagella were measured using line scans. The strong linear
13 relationship between the total integrated fluorescence intensity and equilibrium flagellar length
14 ($R^2=0.89$) demonstrates that the total amount of IFT trains within each *Giardia* flagellum scale
15 linearly with length (Figure 5B).

16 *Giardia* axonemes are sensitive to microtubule assembly and disassembly dynamics
17 during interphase. This offers another opportunity to evaluate the balance point model for
18 length control in *Giardia*, because unlike other model systems (Wang et al., 2013), treatment
19 with the microtubule-stabilizing drug Taxol rapidly increases all flagellar lengths (Dawson et al.,
20 2007). Presumably, the pharmacological treatment with Taxol limits the frequency of
21 catastrophe events at the dynamic plus-end of the microtubules in the axoneme (Dawson et al.,

1 2007). Because we have shown that flagellar length scales with the total amount of IFT trains at
2 equilibrium (Figure 5), we were able to test the response of the *Giardia*'s flagellar length
3 control system to length perturbations in each flagellum induced by Taxol treatment (Figure 5
4 C-E). Treating trophozoites with 20 μ M Taxol for one hour increased the average equilibrium
5 flagellar length by 33% (Figure 5C, D). Specifically, the longer anterior flagella increased in
6 length by 19%, the posteriolateral flagella by 27%, and shorter caudal flagella by 61% (Figure
7 5D). Following Taxol treatment, we again used line scans to quantify the total fluorescence
8 intensity of IFT trains and the lengths of each flagellum (Figure 5C, 5E). The direct relationship
9 between the total amount of IFT trains in each flagellum and its length was unchanged with
10 Taxol treatment (Figure 5E), further supporting the length-independent rates of IFT injection in
11 *Giardia*.

12

13 ***Four different flagellar lengths are maintained by length-dependent disassembly***

14 The balance point model of flagellar length control requires length dependence of either
15 assembly and disassembly rates to achieve overall length control (Mohapatra et al., 2016). In
16 *Chlamydomonas* and *Tetrahymena* length control is achieved through length-dependent IFT
17 assembly with length-independent disassembly (Engel et al., 2009; Vasudevan et al., 2015). As
18 we were unable to confirm length-dependent IFT-mediated assembly for the four *Giardia*
19 flagellar pairs, we also investigated the potential contribution of length-dependent disassembly
20 to the maintenance of four different equilibrium lengths. *Giardia* has a single kinesin-13
21 homolog that localizes to all distal flagellar tips, the median body, and the two mitotic spindles

1 (Dawson et al., 2007). We have shown that kinesin-13 modulates flagellar disassembly in
2 *Giardia*, as the overexpression of a dominant negative kinesin-13 rigor mutant and the
3 depletion of kinesin-13 by CRISPRi-mediated knockdown cause increased flagellar lengths
4 (Dawson et al., 2007; McNally et al., 2019).

5 To assess the contributions of kinesin-13 mediated disassembly to the maintenance of
6 the lengths of all four flagellar pairs, we quantified all flagellar lengths in the CRISPRi-mediated
7 kinesin-13 knockdown (K13kd) strain (Figure 6A, 6B). Using this K13kd strain, we have
8 previously shown that caudal flagellar length increases (McNally et al., 2019). Here we extend
9 this prior work to show that all flagellar pairs have steady-state length increases when kinesin-
10 13 expression is inhibited by ~60% (Figure 6A, 6B) (McNally et al., 2019), consistent with
11 overexpression of a dominant negative rigor kinesin-13 mutant (Dawson et al., 2007).
12 Compared to non-specific gRNA controls, the anterior flagella length in the K13kd strain is
13 increased an average of $1.1 \pm 0.04 \mu\text{m}$, the posteriolateral by $0.9 \pm 0.03 \mu\text{m}$, the caudal by
14 $3.1 \pm 0.18 \mu\text{m}$, and the ventral by $1.6 \pm 0.06 \mu\text{m}$ (Figure 6H).

15 To quantify the localization and turnover dynamics of kinesin-13 along the lengths of all
16 eight flagella, we constructed a fluorescent kinesin-13 fusion strain C-terminally tagged with
17 mNeonGreen (kinesin-13mNG, Figure 6C). Kinesin-13mNG localized to all interphase
18 microtubule structures, including the median body and ventral disc, and to both the
19 cytoplasmic axonemes and the distal flagellar tips of all flagella (Figure 6C). To assess the
20 contribution of kinesin-13-mediated disassembly to the maintenance of flagellar length in
21 *Giardia*, we measured the spatial distribution of fluorescence within the membrane-bound
22 region of the flagellum using line-scans from the flagellar tips to the flagellar pore. The

1 maximum intensity of kinesin-13mNG fluorescence was at the distal region of the flagellar tips
2 and intensity decreases exponentially within the first micrometer from the tip (Figure 6D). The
3 shorter caudal flagella have more kinesin-13mNG at the distal tips than the longer anterior
4 flagella (Figure 6E).

5 The specific localization of kinesin-13 at the distal flagellar tips suggests that this
6 disassembly factor is actively transported to this region, likely via IFT. To characterize kinesin-13
7 transport dynamics, we used FRAP to determine the turnover of kinesin-13 at the distal tips of
8 the caudal and posteriolateral flagella (Figure 6F, Supplemental Video 4). We observed
9 fluorescence recovery of kinesin-13mNG at the distal flagellar tips within two minutes of
10 photobleaching (Figure 6G). Coupled with the observed exponential decay of fluorescence
11 signal from the distal flagellar tip, these findings support that kinesin-13 is transported to the
12 distal flagellar tip.

13

14 ***Distinguishing between two models of disassembly-driven flagellar length control***

15 The dynamic localization of kinesin-13 at the flagellar tips coupled with a length-independent
16 injection rate of IFT supports a length-dependent disassembly length control mechanism in
17 *Giardia*. To further evaluate how a disassembly-driven mechanism involving the depolymerizing
18 kinesin-13 could regulate four different equilibrium flagellar lengths, we developed two
19 alternative models of length control. Both models assume that a higher disassembly rate is
20 conferred by more kinesin-13 localized to shorter flagella (caudal, posteriolateral) than to
21 longer (ventral, anterior) flagella during *de novo* assembly. Both models also propose that

1 kinesin-13 and other cargo are transported to the flagellar tip via anterograde IFT as the
2 flagellum elongates, but that kinesin-13 diffuses back to the flagellar base, independent of
3 retrograde IFT (Figure 8A). Both assumptions are supported by the exponential distribution of
4 kinesin-13 observed in the membrane-bound regions of the flagellum (Figure 6D) and turnover
5 of kinesin-13 following photobleaching (Figure 6G).

6 The two models differ in how the assembly rate changes with the elongation of the
7 flagella. The assembly rate is dependent on both the injection rate of IFT trains and the amount
8 of structural precursor material, presumably tubulin, that remains in the cytoplasmic pool. The
9 “Limited Precursor” model is motivated by length control studies in *Chlamydomonas* where
10 there is a limiting pool of precursor material in the cytoplasm that is shared between the two
11 flagella (Coyne & Rosenbaum, 1970; Marshall et al., 2005). As the flagella elongate the
12 precursor pool is depleted, imparting an assembly rate that is length-dependent and decreases
13 with flagellar length (Figure 7A, 7C). While we show that IFT injection is length-independent,
14 the occupancy of IFT trains by structural components has been shown to vary, so that IFT trains
15 may have cargo-binding sites that are unoccupied during transport (Wren et al., 2013).
16 Therefore, length-independent injection of IFT trains does not necessarily indicate length-
17 independent delivery of structural material to the distal flagellar tip. In the “Excess Precursor”
18 model, there is an excess of precursor material; thus, the assembly rate is length-independent,
19 and this rate remains constant during elongation (Figure 7B, 7D). As per the balance point
20 model, it is the intersection of the assembly and disassembly rates that determine the steady-
21 state length of flagella. Both proposed models achieve control of multiple flagella at distinct
22 lengths (Figure 7C, 7D). However, the models differ in the expected concentrations of kinesin-

1 13 localized to the flagellar tip at equilibrium and during elongation following Taxol treatment.
2 We expect a greater concentration of kinesin-13 at the tips of short flagella in the “Limited
3 Precursor” model, and that the concentration of kinesin-13 will decrease with Taxol elongation
4 (Figure 7C). The “Excess Precursor” model predicts that the concentration of kinesin-13 will be
5 similar between short and long flagella, and that these concentrations will not change with
6 Taxol elongation of flagella (Figure 7D).

7 To distinguish between these two models, we compared the fluorescence intensity of
8 kinesin-13 at the flagellar tip during equilibrium and after flagellar elongation with Taxol (Figure
9 7E, 7F). The degree of flagellar length elongation with Taxol treatment was similar to prior
10 measurements (Figure 5D, Supplemental Figure 4). We also plotted the fluorescence intensity
11 of kinesin-13mNG versus the length of the flagellum (Supplemental Figure 4), and determined
12 that there are no statistically significant differences between the fluorescence intensity of
13 kinesin-13mNG at the flagellar tip at equilibrium or during Taxol elongation (Figure 7F), as
14 predicted by the “Excess Precursor” model (Figure 7D). In the “Excess Precursor” model, the
15 flagellum with more kinesin-13 at the base during *de novo* assembly balances the assembly rate
16 at a shorter length than the flagellum with less kinesin-13 (Figure 7D).

17

18 **Discussion**

19 Multiciliated *Giardia* trophozoites are a unique model in which to test how IFT-mediated
20 assembly and disassembly mechanisms of flagellar length control enable different flagellar
21 lengths in the same multiciliated cell. Like many model organisms, *Giardia* has canonical motile

1 axonemes that are nucleated by basal bodies and have a conserved 9+2 axoneme structure.
2 *Giardia* also possesses the majority of IFT, BBSome, and motor proteins (kinesin-2, kinesin-13,
3 and IFT dynein) that are essential components of flagellar length control mechanisms in diverse
4 model systems (Avidor-Reiss & Leroux, 2015; Lechtreck, 2015). Yet in contrast to other models,
5 the eight *Giardia* axonemes are paired into four flagellar types with four different equilibrium
6 lengths that include long, non-membrane-bound cytoplasmic regions. Flagellar beating of the
7 different flagellar types is essential in *Giardia's* life cycle for motility, cytokinesis, and
8 excystation (Buchel, Gorenflot, Chochillon, Savel, & Gobert, 1987; Hardin et al., 2017;
9 Lenaghan, Davis, Henson, Zhang, & Zhang, 2011). Each flagellar pair also has associated
10 structural elements: the ventral flagella are associated with a fin-like density, the anterior and
11 posteriolateral flagella have associated electron dense structures along their cytoplasmic
12 regions, and the caudal complex surrounds the cytoplasmic regions of the caudal flagella
13 (Elmendorf, Dawson, & McCaffery, 2003).

14 We demonstrate two types of evolutionary innovations in *Giardia* that may be broadly
15 generalizable to other eukaryotes that generate variation in both axonemal architecture and in
16 flagellar length regulation in multiciliated cells. First, while all *Giardia* flagella lack transition
17 zone regions, each axoneme retains an analogous diffusion barrier defined by the eight flagellar
18 pores to create a compartmentalized flagellum. This barrier has a similar function to the TZ but
19 is not associated with basal bodies and is likely not homologous as the flagellar pore lacks TZ
20 protein homologs. The second innovation enables four flagella of different lengths, and is a
21 modification of flagellar length regulatory mechanisms, wherein kinesin-13 mediated

1 disassembly rates are dependent on flagellar length, but IFT-mediated assembly rates are
2 length-independent.

3 ***Eight flagellar pores are cytoplasmic diffusion barriers analogous to the transition zone***

4 The central cytoplasmic location of the eight basal bodies between the two nuclei is an atypical
5 aspect of diplomonads like *Giardia*. In bi-flagellated *Chlamydomonas*, the basal bodies are
6 anchored to the plasma membrane by transition zone fibers (Reiter et al., 2012). IFT particles
7 (trains) are specialized for specific molecular cargos needed to build the growing axoneme. IFT
8 trains accumulate in the transition zone, where they are loaded with axonemal structural
9 material and transported to the distal flagellar tip by the heterotrimeric kinesin-2 complex
10 (Deane, Cole, Seeley, Diener, & Rosenbaum, 2001; Wingfield et al., 2017). Retrograde trains are
11 returned from the distal tip back to the cell body by cytoplasmic dynein (Pazour, Dickert, &
12 Witman, 1999). Together, these motor-IFT complexes mediate dynamic trafficking of structural
13 and signaling proteins into the compartmentalized flagellum, and are required for both flagellar
14 assembly and maintenance (Lechtreck, 2015; Reiter et al., 2012). Regulation of IFT particle
15 assembly, including regulation of motors and ultimately, flagellar length, is commonly
16 attributed to regulatory proteins localizing to the transition zone. Thus the lack of a transition
17 zone – known to both compartmentalize and concentrate proteins within the cilium – poses a
18 conundrum in *Giardia*: how and where are IFT particles loaded and injected into the
19 membrane-bound flagellar compartments (Avidor-Reiss & Leroux, 2015; Barker et al., 2014)?

20 Despite our prior analyses of flagellar assembly and disassembly in *Giardia* (Dawson et
21 al., 2007; Hoeng et al., 2008), it has remained unclear where IFT particles assemble, mature,

1 and are injected into the membrane-bound axonemal regions. Through GFP-tagging and
2 imaging all IFT homologs in *Giardia*, we confirmed that all anterograde and retrograde IFT
3 components localize not only to the membrane bound regions of axonemes, but also densely
4 localize to the non-membrane-bound cytoplasmic regions (Figure 2). IFT particles also
5 concentrate at each of the eight flagellar pores – the interface between the cytosol and
6 compartmentalized membrane-bound axonemes (Figure 2A and (Hoeng et al., 2008)).
7 Anterograde kinesin-2a and kinesin-2b motors also accumulate at each of the flagellar pores
8 and flagellar tips, yet they lack a similar intensity of localization to the cytoplasmic regions of
9 axonemes or basal bodies. The accumulation (Figure 2C) and turnover (Figure 3B, 3D) of IFT
10 proteins at the flagellar pores result from the mixing of IFT particles from two sources: diffusive
11 IFT particles from the cytoplasmic axonemal regions and IFT trains as they return via retrograde
12 transport (Figure 3F). We propose that immature IFT particles first associate with cytoplasmic
13 axonemal regions and mature at the eight flagellar pores, prior to their injection into the
14 compartmentalized, membrane-bound axonemal region.

15 Thus, the eight flagellar pore regions act as a diffusion barrier between the cytoplasmic
16 and membrane bound axoneme regions, resulting in the compartmentalization of the
17 membrane-bound regions of the eight flagella. The mechanism by which the flagellar pores act
18 as cytoplasmic diffusion barriers and regulate IFT injection is likely is analogous to that in other
19 flagellates, yet in the absence of a TZ, *Giardia* must employ alternative or novel components.
20 Overall, the TZ-independent accumulation and injection of IFT particles in *Giardia* demonstrates
21 that eukaryotic flagella can be compartmentalized to concentrate proteins within the flagellar
22 compartment in the absence of the canonical TZ complex, and thus raises questions regarding

1 the necessity of this complex for IFT-mediated assembly in other flagellates. Further
2 characterization of the ultrastructure and the composition of the flagellar pore complex in
3 *Giardia* will be key to determining how this complex mediates compartmentalization and
4 regulates IFT injection. The cytoplasmic face of pore complex also may play a role in directing
5 the cytoplasmic axonemes to their defined exit points at the flagellar pores.

6 Other flagellated organisms lack IFT or TZ components and use IFT-independent or
7 compartment-independent mechanisms to assemble flagella (Avidor-Reiss & Leroux, 2015), yet
8 *Giardia's* flagella appear to use a unique variation of these mechanisms. While an essential role
9 for the TZ has been implied for many flagellates, there are several ciliated protozoans of the
10 phylum *Apicomplexa* (e.g., *Plasmodium*, *Toxoplasma*) that also lack a transition zone structure.
11 These apicomplexans, however, are thought to rely entirely on cytoplasmic ciliogenesis and do
12 not possess compartmentalized flagella (Avidor-Reiss & Leroux, 2015). Other flagellated cells
13 use both cytosolic and compartmentalized ciliogenesis, which creates two spatially distinct
14 regions of the organelle that likely require unique assembly and maintenance dynamics. These
15 observations support a mechanism of ciliogenesis that is not diffusion-limited and therefore
16 does not require IFT for assembly of the cytoplasmic axonemal regions. Both mammalian and
17 *Drosophila* sperm flagella employ variations of cytoplasmic ciliogenesis that require the
18 invagination of the basal body into the cytoplasm following the initiation of compartmentalized
19 ciliogenesis (Avidor-Reiss et al., 2017).

20 As in other eukaryotes with IFT-mediated flagellar assembly, conserved IFT components
21 (e.g., IFT trains, BBsome, and kinesin and dynein motors) assemble the membrane-bound
22 regions of each the eight *Giardia* axonemes (Hoeng et al., 2008; McNally et al., 2019).

1 Cytoplasmic regions of each axoneme may be assembled in an IFT-independent manner as
2 neither kinesin-2 knockdown nor expression of a dominant negative kinesin-2 affect
3 cytoplasmic axoneme length (Dawson et al., 2007; Hoeng et al., 2008). Additionally, the
4 cytoplasmic regions of the caudal and anterior axonemes of each daughter are proposed to be
5 structurally inherited from the parental cell and are associated with mother, grandmother, and
6 great-grandmother basal bodies (Nohynková et al., 2006). The two other flagellar pairs (ventral
7 and posteriolateral) arise from *de novo* assembly immediately following cell division (Hardin et
8 al., 2017; Sagolla, Dawson, Mancuso, & Cande, 2006). While we have not directly imaged the
9 assembly of the cytoplasmic axonemal regions in this study, the lack of transport of IFT particles
10 and kinesin-2 localization on cytoplasmic regions during interphase support an IFT-independent
11 mechanism of flagellar assembly of the two *de novo* flagellar pairs (posteriolateral and ventral).
12 This mode of ciliogenesis appears similar to that of *Plasmodium*, which occurs entirely in the
13 cytoplasm with no membrane invagination or basal body migration in the absence of all known
14 IFT components, including the transition zone and the BBSome (Avidor-Reiss & Leroux, 2015;
15 Barker et al., 2014). The necessity of cytoplasmic ciliogenesis to precede the assembly of the
16 membrane bound regions could essentially make the TZ dispensable in *Giardia*.

17

18 ***Length-independent IFT-mediated assembly of all eight membrane-bound flagella***

19 To set the length of a dynamic structure at a specific size, the rate of subunit addition must be
20 balanced by the rate of subunit removal (Marshall et al., 2005; Mohapatra et al., 2016). The
21 prevailing balance-point model of flagellar length control proposes that equilibrium length is

1 achieved through the balance of assembly and disassembly rates (Engel et al., 2009; Ludington,
2 Wemmer, Lehtreck, Witman, & Marshall, 2013; Mohapatra et al., 2016). The flagellar assembly
3 rate is thus a result of IFT train injection into the membrane-bound region of the flagellum. IFT-
4 mediated assembly is thought to be length-dependent as the size and number of IFT injections
5 is inversely correlated with flagellar length (Engel et al., 2009). In contrast, the disassembly rate
6 is thought to be length-independent (Engel et al., 2009; Ludington et al., 2013). Length-
7 dependent assembly is proposed to arise from the depletion of the assembly motor, kinesin-2,
8 at the flagellar base and the diffusive return of this essential IFT component from the flagella tip
9 (Chien et al., 2017; Fai, Mohapatra, Kondev, & Amir, 2019; Hendel et al., 2018). In this way, the
10 amount of kinesin-2 available to be incorporated into IFT trains acts as a length-ruler of flagella.

11 Again, the existence of eight flagella of four different equilibrium lengths (Figure 1)
12 poses a challenge to the canonical model of flagellar length control. Based on the balance point
13 model, one might predict that *Giardia* differentially regulates flagellar assembly amongst
14 flagella of different lengths by differentially regulating IFT dynamics (particle size, number, or
15 injection frequency). Yet we show here that IFT dynamics and IFT train injection are consistent
16 between flagella of different equilibrium lengths (Figures 4, 5). Furthermore, this injection rate
17 remains constant with increased flagellar length pharmacologically induced by Taxol treatment
18 (Figure 5E). These observations imply that tuning of assembly rates is not a regulatory
19 mechanism used to maintain differential lengths for different flagellar pairs in *Giardia*. The
20 length-independent assembly of *Giardia* axonemes contrasts with observations in the green
21 alga *Chlamydomonas reinhardtii*, wherein IFT train injection decreases with increasing flagellar
22 length, therefore providing a length-dependent assembly rate (Chien et al., 2017; Hendel et al.,

1 2018). Several kinases are known to regulate either assembly or disassembly rates in
2 *Tetrahymena* and *Chlamydomonas* (CALK, LF4, Nrks/Neks), and *Giardia* has 198 Nek proteins
3 whose functions are yet to be determined (Berman, Wilson, Haas, & Lefebvre, 2003; Bradley &
4 Quarmby, 2005; Hilton, Gunawardane, Kim, Schwarz, & Quarmby, 2013; Manning et al., 2011;
5 Meng & Pan, 2016; Wloga et al., 2006).

6

7 ***Differential, length-dependent disassembly results in flagella of differing lengths***

8 Kinesin-8 and kinesin-13 are depolymerizers of cytoplasmic, spindle, and ciliary microtubule
9 ends (Helenius, Brouhard, Kalaidzidis, Diez, & Howard, 2006; Walczak, Gayek, Ohi, &
10 Wordeman, 2013). Kinesin-13 depolymerizes the ends of microtubules via ATP hydrolysis and
11 can traffic to microtubule ends by diffusion, by plus end-tracking proteins or by motors (Cooper
12 & Schafer, 2000; Desai, Verma, Mitchison, & Walczak, 1999; Honnappa et al., 2009; Li et al.,
13 2009). *Giardia* has a single kinesin-13 homolog that regulates dynamics of various MT arrays
14 (e.g., two spindles, median body MTs, and axonemes). This is unlike metazoans, *Tetrahymena*,
15 and trypanosomes, all of which have multiple kinesin-13 homologs with duplicated or
16 differentiated functions in the various arrays. In *Giardia*, the ectopic expression of a dominant-
17 negative, kinesin-13 rigor mutant or CRISPRi-mediated knockdown of kinesin-13 (Figure 6)
18 results in dramatically longer flagella (Dawson et al., 2007; McNally et al., 2019). The
19 ultrastructure of the all eight axonemes retain the canonical 9+2 arrangement of doublet
20 microtubules but lack a flagellar tip complex (Dawson et al., 2007). Equilibrium flagellar lengths
21 in *Giardia* are also sensitive to drugs that impact MT dynamics, and flagellar lengths are also

1 increased by limiting MT catastrophes through treatment with the MT stabilizing drug Taxol
2 (Dawson et al., 2007). Intrinsic microtubule dynamics may have a more pronounced
3 contribution to flagellar length control in *Giardia* than in metazoans and *Chlamydomonas* as
4 these flagella are comparatively less sensitive to microtubule stabilizing and destabilizing drugs
5 (Wang et al., 2013).

6 Kinesin-13 contributions to flagellar assembly and disassembly have also been
7 investigated in other microbial flagellates such as *Leishmania*, *Tetrahymena*, and
8 *Chlamydomonas* (Blaineau et al., 2007; Chan & Ersfeld, 2010; Li et al., 2009; Vasudevan et al.,
9 2015; Wang et al., 2013). Kinesin-13 has a similar role in mediating axoneme disassembly in
10 *Leishmania*, where the knockdown of one (of the seven) kinesin-13 homologs promotes
11 increased flagellar length, and overexpression of the same kinesin-13 homolog results
12 decreased flagellar length (Blaineau et al., 2007). Depletion of the sole kinesin-13 in
13 *Chlamydomonas* results in shorter flagella due to the depletion of the cytoplasmic tubulin pool
14 required for IFT-mediated assembly, and also results in the disassembly of axonemes through
15 IFT transport of kinesin-13 to the distal flagellar tip during the induction of flagellar resorption
16 (Li et al., 2009; Wang et al., 2013). In *Tetrahymena* however, cell body MTs are shortened by
17 kinesin-13, but this activity is not required for liberating ciliary precursor tubulin. Thus, in some
18 flagellated cells, rather than directly playing a role in flagellar disassembly, kinesin-13 may
19 indirectly impact flagellar IFT-mediated assembly, and ultimately flagellar length, through its
20 role in the modulation of cytoplasmic tubulin precursor pools.

21 In *Giardia*, kinesin-13 also localizes to the median body, a centrally located cytoplasmic
22 MT array, and to the kinetochore MTs of two mitotic spindles (Dawson et al., 2007). The

1 median body is a semi-organized interphase MT array that is proposed to act as a cytoplasmic
2 reservoir of tubulin prior to cell division (Hardin et al., 2017). Median body MTs are dynamic,
3 and are sensitive to drugs that affect MT dynamics (Dawson et al., 2007). Over-expression of
4 the kinesin-13 rigor mutant also results in decreases in median body volume (Dawson et al.,
5 2007). In addition to regulating MT dynamics at the flagellar tips, kinesin-13 also regulates
6 cytoplasmic tubulin pools through liberation of tubulin subunits in the median body in *Giardia*.

7 In the absence of differences in length-dependent axoneme assembly, we investigated
8 the contribution of flagellar disassembly to flagellar length control in *Giardia*. Kinesin-13
9 dynamically localizes to the distal flagellar tip of all flagellar pairs, which is consistent with
10 kinesin-13 depolymerizing in a length-dependent manner. In the absence of other active
11 transport mechanisms within the membrane-bound flagellum, we propose that kinesin-13 is a
12 cargo of IFT (Li et al., 2009). Due to turnover of kinesin-13 at the distal flagellar tip, coupled
13 with the apparent exponential distribution of kinesin-13 fluorescence intensity within the
14 flagellum, we suggest that kinesin-13 activity is a primary driver of differential flagellar length
15 regulation in *Giardia* (Figure 8).

16

17 ***A disassembly mediated model for flagellar length control***

18 *Giardia* tunes differential flagellar lengths through the modulation of axonemal-specific, length-
19 dependent flagellar disassembly rates, rather than length-dependent IFT-mediated assembly
20 rates as reported in other systems (Figure 8C). The four equilibrium flagellar lengths are
21 achieved by modulating the amount of kinesin-13 accumulated to the distal flagellar tip during

1 assembly (Figure 8C); however, it remains unclear how kinesin-13 is differentially transported
2 or regulated at the eight different flagellar tips.

3 Generally, we propose that kinesin-13 is transported to the distal flagellar tips by IFT,
4 where it is released from the IFT train and can interact with the flagellar axoneme to promote
5 disassembly. When unbound from the axoneme, kinesin-13 diffuses back toward the flagellar
6 pores, similar to kinesin-2 (Chien et al., 2017; Hendel et al., 2018). During this diffusion, kinesin-
7 13 can rebind to an anterograde IFT train, preventing the “escape” of kinesin-13 from the distal
8 flagellar tip and generating the observed distribution and tip accumulation within the flagellar
9 compartment (Figure 8A). Importantly, this model of flagellar length assembly and maintenance
10 generates specific predictions about the intensity profiles of the various IFT components within
11 the membrane-bound region of the flagellum. Components that undergo anterograde and
12 retrograde transport (IFT-A, IFT-B, IFT dynein) are expected to display a uniform fluorescence
13 distribution within the membrane-bound flagellum (Figure 8B). Anterograde transport coupled
14 with retrograde diffusion produces a linear decrease in fluorescence signal intensity and would
15 be expected for kinesin-2 (Figure 8B, (Chien et al., 2017; Hendel et al., 2018)). Lastly, we
16 propose that components which undergo anterograde transport with retrograde diffusion and
17 recapture by anterograde complexes are expected to display an exponential decrease in
18 fluorescence signal (Naoz, Manor, Sakaguchi, Kachar, & Gov, 2008), as is observed with kinesin-
19 13 (Figure 8B).

20 Both between species and even within cell types of the same species, eukaryotic cells
21 have diverse cytoskeletal architectures that enable innovations in motility and other cellular
22 functions. Defining the molecular mechanisms by which non-canonical flagellated cells like

1 *Giardia* alter the balance of well-studied IFT assembly and kinesin-13 mediated disassembly
2 mechanisms illuminates how cells can evolve varied morphological forms. Beyond microbial
3 flagellates, we expect the mechanistic and structural innovations we describe in *Giardia* will
4 echo well-described variations in flagellar structure, type, and number found in different cell
5 types in humans and other multicellular model systems.

6

7 **Methods**

8 ***Strains and culture conditions***

9 *Giardia lamblia* (ATCC 50803) strains were cultured in modified TYI-S-33 medium supplemented
10 with bovine bile and 5% adult and 5% fetal bovine serum [56] in sterile 16 ml screw-capped
11 disposable tubes (BD Falcon). Cultures were incubated upright at 37°C without shaking as
12 previously described(Hagen et al., 2011). GFP and mNeonGreen-tagged IFT strains were created
13 by electroporation of episomal vectors into strain WBC6 using approximately 20 µg plasmid
14 DNA (Hagen et al., 2011). Tagged strains were maintained with antibiotic selection (50 µg/ml
15 puromycin and/or 600 µg/ml G418)(Hagen et al., 2011). Trophozoites treated with Taxol were
16 grown to confluency and split into 6 ml culture tubes 2 hours prior to incubation with Taxol
17 (20µM final concentration) or DMSO (0.2% final concentration) for one hour. Live or fixed
18 imaging was performed as described below.

19 ***Construction of episomal and integrated C-terminal GFP and mNeonGreen-tagged IFT strains***

1 Eleven intraflagellar transport (IFT) homologs were identified by homology searches in the
2 *Giardia* genome (GL50803) using GiardiaDB (Aurrecochea et al., 2009). C-terminal GFP tagged
3 IFT homologs were created by PCR amplification of genomic DNA (Table 2) and subsequent
4 cloning of the IFT homolog amplicons into a *Giardia* Gateway cloning vector (Hagen et al.,
5 2011). For live imaging of IFT particles, we constructed an IFT81mNeonGreen strain by PCR
6 amplification of the IFT81 gene (GL50803_15428) (Table2) to generate IFT81 flanked by 5' NotI
7 and 3' BamHI restriction sites. The resulting amplicon was gel purified using a Zymoclean Gel
8 DNA Recovery kit (Zymo Research) and cloned into pKS_mNeonGreen-N11_PAC (Hardin et al.,
9 2017; Shaner et al., 2013) using Gibson cloning (Gibson et al., 2009). The resulting
10 IFT81mNeonGreen and IFT81GFP plasmids were linearized with AflIII for integration into the
11 native locus (Gourguechon & Cande, 2011). To verify integration, total genomic DNA was
12 extracted from tagged IFT81 strains using DNA STAT-60 (Tel-Test, Inc.), and integration of the C-
13 terminal tag was confirmed by PCR amplification (Supplemental Figure 2).

14 ***Immunostaining and light microscopy***

15 *Giardia* trophozoites were grown to confluency as described above. Media was then replaced
16 with 1x HBS (37°C), and the cultures were incubated at 37°C for 30 minutes. To detach and
17 harvest cells, culture tubes were incubated on ice for 15 minutes and centrifuged at 900 x g, 4°C
18 for five minutes. Pellets were washed twice with 6 ml cold 1x HBS and resuspended in 500 µl 1x
19 HBS. Cells (250 µl) were attached to warm coverslips (37°C, 20 min), fixed in 4%
20 paraformaldehyde, pH 7.4 (37°C, 15 min), washed three times with 2 ml PEM, pH 6.9 (Woessner
21 & Dawson, 2012) and incubated in 0.125M glycine (15 min, 25°C) to quench background
22 fluorescence. Coverslips were washed three more times with PEM and permeabilized with 0.1%

1 Triton X-100 for 10 minutes. After three additional PEM washes, coverslips were blocked in 2 ml
2 PEMBALG (Woessner & Dawson, 2012) for 30 minutes and incubated overnight at 4°C with anti-
3 TAT1 (1:250) and/or anti-GFP (1:500, Sigma) antibodies. The following day, coverslips were
4 washed three times in PEMBALG and then incubated with Alexa Fluor 555 goat anti-rabbit IgG
5 (1:1000; Life Technologies), Alex Fluor 594 goat anti-mouse antibodies (1:250; Life
6 Technologies) and/or Alex Fluor 647 goat anti-mouse (1:250; Life Technologies) antibodies for 2
7 hours at room temperature. Coverslips were washed three times each with PEMBALG and PEM
8 and mounted in Prolong Gold antifade reagent with DAPI (Life Technologies).

9 ***Flagellar pair length measurements***

10 *Giardia* trophozoites were fixed and stained with TAT1 (1:250) and Alexa Fluor 594 goat anti-
11 mouse IgG (1:250; Life Technologies) as described above. For flagellar pair length
12 measurements, serial sections of immunostained trophozoites were acquired at 0.2 μm
13 intervals using a Leica DMI 6000 wide-field inverted fluorescence microscope with a PlanApo
14 $\times 100$, 1.40 numerical aperture (NA) oil-immersion objective. DIC images were analyzed in FIJI
15 (Schindelin et al., 2012) using a spline-fit line to trace the flagella from the cell body to the
16 flagellar tip. Flagellar length measurements were analyzed and quantified using custom Python
17 scripts. $n \geq 35$ flagella for each pair. Flagellar length data are shown as mean relative length
18 changes with 95% confidence intervals.

19 ***Live imaging of IFT in Giardia***

20 For live imaging, strains were grown to confluency, incubated on ice for 15 minutes to detach
21 cells and pelleted at 900 x g for five minutes at 4°C. Cell pellets were washed three times in 6

1 mL of cold 1x HBS. After the final wash, cells were resuspended in 1mL of cold 1x HBS. For live
imaging, 500 μ L of washed trophozoites were added to the center of a prewarmed 35 mm
imaging dish (MatTek Corporation) and incubated for 20 minutes at 37°C. The imaging dish was
washed with three times with warmed 1x HBS to remove unattached cells. For some
experiments, CellMask Deep Red plasma membrane stain (ThermoFisher) was used to label the
cell membrane (1x final concentration, 15 minutes at 37°C). Attached cells were embedded in
1mL 3% low melt agarose (USB Corporation) in 1x HBS (37°C) to limit flagellar beating and
prevent detachment. The imaging dish was sealed using parafilm and imaged on a 3i spinning
disc confocal microscope (Intelligent Imaging Innovations, Inc.).

10 ***Quantification of IFT81mNG full axoneme fluorescence intensity***

11 For analysis of IFT along the entire length of axonemes (basal body to flagellar tip), the
12 IFT81mNG strain was grown to confluency and prepared for live imaging (see above). Images
13 were acquired on a 3i spinning disc confocal microscope as described below. The segmented
14 line tool in FIJI was used to measure the fluorescence intensity along the entire axoneme from
15 basal body to the flagellar tip. Quantification was conducted for the anterior and posteriolateral
16 flagella from 31 cells acquired in three independent experiments. The overall distance from the
17 basal body to the flagellar pore and the flagellar tip was also recorded for each cell. Python
18 scripts were used to plot the mean intensity for all analyzed cells and to calculate and plot the
19 95% confidence interval for all measurements.

20 ***Fluorescence recovery after photobleaching (FRAP)***

1 To quantify IFT dynamics at different regions of axonemes, the integrated IFT81mNeonGreen
2 strain was grown to confluency and prepared for live imaging as described above. Images were
3 acquired using a 3i spinning disc confocal microscope (Intelligent Imaging Innovations, Inc.)
4 using a 63x, 1.3 NA objective. The microscope was warmed to 37°C one hour prior to image
5 acquisition to maintain cells at physiological temperature and DefiniteFocus (Zeiss) was used to
6 prevent drift during image acquisition. Either the cytoplasmic axoneme region or the flagellar
7 pore region of the posteriolateral flagellum was bleached using Vector (Intelligent Imaging
8 Innovations, Inc.) with a 488nm laser (10% laser power, 5ms exposure). To monitor recovery,
9 images were acquired with a 488nm laser (50ms exposure and 50% laser power on gain set to 2
10 with intensification set to 667) at one-second intervals. Images were processed using the
11 Template Matching plugin for FIJI to correct drift during acquisition. Once corrected for drift,
12 ROIs were identified, and intensity measurements were recorded for each experimental time
13 point. Background intensity measurements were taken for each cell analyzed from an adjacent
14 area with no detectable fluorescence. Photobleaching measurements were taken from a non-
15 bleached region of the cell analyzed. Quantification of fluorescence recovery was performed
16 using custom Python scripts to subtract background intensity and correct for photo-bleaching.
17 Individual recoveries were fit using Equation 1 (Ellenberg et al., 1997) to measure the diffusion
18 constant:

19 (1)
$$I_{CA}(t) = I_0 \left(1 - \sqrt{\frac{\omega^2}{\omega^2 - 4\pi Dt}} \right)$$

20 where $I_{CA}(t)$ is the intensity as a function of time and zero time is bleaching event; I_0 is the
21 final intensity after recovery; ω is the bleach strip width; D is the diffusion constant.

1 At short times, Equation 1 becomes Equation 2:

2
$$(2) I_{CA}(t) = I_0 \frac{2\pi Dt}{\omega_{CA}^2}$$

3 where ω_{CA} is the bleach strip width for the cytoplasmic axoneme. To predict the initial recovery
4 of the flagellar pore region, the flux from retrograde IFT transport is added to Equation 2:

5
$$(3) I_{FP}(t) = I_0 \left(\frac{2\pi Dt}{\omega_{CA}^2} + \frac{\lambda_0}{C_0} \frac{v}{\omega_{FP}} \right) t$$

6 where $I_{FP}(t)$ is the intensity as a function of time; $\frac{\lambda_0}{C_0}$ is the relative difference in integrated
7 fluorescence intensity in the membrane-bound axoneme and the cytoplasmic axoneme; v is the
8 speed of retrograde IFT; and ω_{FP} is the width of the bleach strip for the flagellar pore. Inputting
9 all measured parameters into Eqs 2 and 3 predicts that $\frac{I_{FP}}{I_{CA}} = 3 \pm 1$ for the initial period of
10 recovery. Fits of the initial linear phase of recovery were conducted using linear regression.

11 All recovery measurements (32 cytoplasmic axonemes and 25 flagellar pores, from at least 3
12 independent experiments) were average and rescaled based on the average initial intensity and
13 bleach depth.

14 ***IFT particle tracking using kymograph analysis***

15 To track IFT train traffic in live cells, the integrated IFT81mNeonGreen strain was first grown to
16 confluency and then prepared for live imaging as described above. Images were acquired using
17 a 3i spinning disc confocal microscope (Intelligent Imaging Innovations, Inc.) using a 100x, 1.46
18 NA objective (330 images, 30ms exposure, intensification = 667, and gain = 2; the total time was
19 about 26 seconds for each acquisition for a frame rate of approximately 13fps). The microscope

1 was warmed to 37°C one hour prior to image acquisition to maintain cells at physiological
2 temperature and DefiniteFocus (Zeiss) was used to prevent drift during image acquisition.
3 Kymographs were generated using the KymographClear 2.0 plugin for FIJI (Mangeol et al.,
4 2016). A maximum intensity projection image was generated from the time lapse series to
5 identify flagella, and a segmented, spline-fit line was used to trace identified flagella in the
6 time-lapse images. Kymographs were generated for cells that had at least two identified flagella
7 from different flagellar pairs to make intracellular comparisons. Intracellular comparisons were
8 made for 22 cells for the anterior and caudal flagella and for 42 cells for the anterior and
9 posteriolateral flagella, obtained from five independent microscopy experiments. Kymographs
10 were analyzed using KymographDirect software with background correction and correction for
11 photobleaching, and data were further analyzed using custom Python scripts.

12 ***IFT injection frequency distributions***

13 Forward-filtered kymographs generated above were used to measure the time-lag between IFT
14 train injections. Using custom Python scripts, we calculated the time between each injection
15 event for anterior, posteriolateral, and caudal flagella. Frequency histograms for each flagellar
16 pair were fit with a single exponential to measure the rate of IFT injection for each flagellar pair.

17 ***Quantification of integrated IFT particle intensity using super-resolution microscopy***

18 The integrated IFT81GFP strain was first grown to confluency, then fixed and stained as
19 described. 3D stacks were collected at 0.125 μ m intervals on a Nikon N-SIM Structured
20 Illumination Super-resolution Microscope with a 100x, 1.49 NA objective, 100 EX V-R diffraction
21 grating, and an Andor iXon3 DU-897E EMCCD. Images were reconstructed in the “Reconstruct

1 Slice" mode and were only used if the reconstruction score was 8. Raw and reconstructed
2 image quality were further assessed using SIMcheck and only images with adequate scores
3 were used for analysis (Ball et al., 2015).

4 To determine intensity profiles along the length of flagellar pairs, we used the maximum
5 intensity projections of reconstructed SIM images for tubulin (anti-TAT) and IFT81GFP (anti-
6 GFP). Intensity measurements from ten different cells from three separate experiments were
7 used. Intensity profiles and flagellar length measurements were measured using FIJI and the
8 total integrated intensity was calculated by determining the total area under the curve (AUC)
9 using custom Python scripts.

10 ***Quantification of kinesin13mNG membrane-bound axoneme fluorescence intensity***

11 Trophozoites expressing kinesin13mNG were prepared for live imaging as above. The
12 segmented, spline-fit line tool in FIJI was used to trace the length of the flagellum, from the tip
13 to the base, and measure the intensity. Measurements from at least 23 cells for each flagellar
14 pair from two independent experiments were used. Only cells with at least two measured
15 flagella were analyzed. Custom Python scripts were used to generate plots and statistical
16 analyses of the data.

17 **Acknowledgements**

18 This work was supported by NIH/NIAID awards 2R01AI077571-10A1 to SCD. JK is funded by the
19 National Science Foundation grants DMR-1610737 and MRSEC-1420382, and by the Simons
20 Foundation. SGM was supported by NIH T32 GM0007377. Plasmid pKS_mNeonGreen-N11_NEO
21 was a gift from Alex Paredez (University of Washington, Seattle). We thank the MCB Light

1 Microscopy Imaging Facility, a UC Davis Campus Core Research Facility, for the use of the 3i
2 spinning disc confocal microscope (Intelligent Imaging Innovations, Inc.) and the N-SIM
3 Structured Illumination Super-resolution Microscope (Nikon). We thank Kari Hagen for valuable
4 editorial assistance and the Physiology course at the Marine Biological Laboratory.

5

6 **Figure legends**

7 Figure 1: *Giardia* maintains four flagellar pairs at unique equilibrium lengths.

8 (A) Schematic representation of membrane-bound, cytoplasmic, basal body (BB), and flagellar
9 pore (fp) regions of the axoneme, as well as the two nuclei (N) and median body (MB). (B)
10 Schematic representation of the specific regions of *Giardia's* flagellar axoneme, including the
11 cytoplasmic axoneme (cytoplasmic), flagellar pore (FP), membrane-bound axoneme
12 (membrane-bound), and the flagellar tip (tip). (C) Fluorescent labeling of the microtubule
13 cytoskeleton and membrane of a *Giardia lamblia* trophozoite, including the median body (MB),
14 the basal body (BB), and the four flagellar pairs: anterior (AF), posteriolateral (PF), caudal (CF),
15 and ventral (VF). Scale bar, 5 μ m. (D) Flagellar length quantification of membrane-bound regions
16 of flagellar pairs of *Giardia* WBC6 trophozoites. The 95% confidence interval and average length
17 are indicated. $n \geq 35$ flagella for each pair. All pairs are statistically significantly different
18 ($p \leq 0.05$, t-test) in membrane-bound length, except the posteriolateral and caudal flagella.

19

20 Figure 2: IFT particles accumulate at the flagellar pore in a flagellum-specific manner.

1 (A) Maximum intensity projections of live cells show the distribution of kinesin-2, BBSome, IFT-
2 A complex, and IFT-B complex proteins throughout the trophozoite. Representative schematic
3 of IFT-A and IFT-B localizations is in the lowest left corner. All scale bars, 5 μ m. (B)
4 IFT81mNeonGreen proteins are more concentrated at the flagellar pore regions of the flagellar
5 pairs. Scale bar, 5 μ m. (C) Quantification of IFT81mNG distribution along the entire lengths of
6 anterior and posteriolateral axonemes using line-scans. Black lines indicate mean intensity and
7 shaded regions indicate 95% confidence intervals. Flagellar length is indicated on bottom axis
8 and relative anatomical position is indicated on the top axis, with red shading indicating the
9 flagellar pore region. n = 31 for each flagellar pair, from four independent experiments.

10

11 Figure 3: IFT train assembly occurs at the flagellar pore region.

12 (A) Time series images of trophozoites expressing IFT81mNG prebleach, immediately post-
13 bleach (0 sec, yellow arrow) of cytoplasmic axoneme or (B) flagellar pore regions, and during
14 recovery (time in sec). Scale bar, 2 μ m. (C) Time averaged fluorescent recovery of posteriolateral
15 cytoplasmic axonemes and (D) flagellar pores. Solid black lines indicate fit of the entire recovery
16 phase. Dashed lines indicate linear fit of the initial recovery phase. n = 32 for bleached
17 cytoplasmic axoneme regions, n = 25 for bleached flagellar pore regions, each from 3
18 independent experiments. (E) Estimated diffusion constants from fitting FRAP recovery of the
19 flagellar pore and cytoplasmic regions of posteriolateral flagella. Means and 95% confidence
20 intervals are indicated. Student's t-test, **p<0.01. n \geq 25 cells, from \geq 3 independent

1 experiments. (F) Schematic representation of IFT particle behavior associated with the
2 cytoplasmic axoneme, flagellar pore, and membrane-bound axoneme regions.

3

4 Figure 4: IFT dynamics are similar between flagellar pairs of different lengths.

5 (A) Still images from time-lapse imaging of live trophozoites expressing IFT81mNG showing
6 anterograde (magenta arrows) and retrograde IFT trains (green arrows). Scale bar, 2 μ m. (B) A
7 representative kymograph of IFT train trajectories within the membrane-bound anterior
8 flagellum. Total time is \sim 26 sec. Scale bar, 1 μ m and 1 second. (C) Comparisons of anterograde
9 IFT train intensity, frequency, and speed from anterior and caudal flagella. (D) Comparisons of
10 anterograde IFT train intensity, frequency, and speed from anterior and posteriolateral flagella.
11 (E) Comparisons of retrograde IFT train intensity, frequency, and speed from anterior and
12 caudal flagella. (F) Comparisons of retrograde IFT train intensity, frequency, and speed from
13 anterior and posteriolateral flagella. All plots show mean values with 95% confidence intervals.
14 Student's t-test, * $p < 0.05$. $n = 22$ cells for the anterior and caudal flagella, $n = 42$ cells for the
15 anterior and posteriolateral flagella, from $N = 5$ independent experiments. (G) Frequency
16 histograms of the time-lag between IFT train injections for anterior (blue), posteriolateral
17 (green), and caudal (orange) flagella. Black line indicates a fit to a single exponential equation to
18 measure the injection rate for each flagellar pair. Injection rates are indicated with 95%
19 confidence intervals.

20

21 Figure 5: IFT injection is length-independent.

1 (A) Representative structured illumination microscopy (SIM) image of IFT81GFP (green)
2 immunostained for α -tubulin (magenta) and stained with DAPI (blue). Scale bar, 2 μ m. Boxed
3 inset is enlarged on the right. Scale bar, 0.5 μ m. (B) Total integrated intensity of IFT81GFP
4 trophozoites plotted versus flagellar length. Orange dots indicate caudal flagella, green dots
5 indicate posteriolateral flagella, and blue dots indicate anterior flagella. Linear fit (black line)
6 and coefficient of determination are indicated. Shading indicates 95% confidence interval. (C)
7 Representative SIM images of IFT81GFP trophozoites treated with DMSO (left) or 20 μ M Taxol
8 (right) for 1 hour, then fixed and stained as in A. (D) Flagellar length of IFT81GFP trophozoites
9 treated with DMSO (gray) or 20 μ M Taxol (red). Ten cells from three separate experiments were
10 measured for each condition. Student's t-test, ***p<0.001. (E) Total integrated intensity of
11 IFT81GFP trophozoites treated with DMSO (gray) or 20 μ M Taxol (red) plotted versus flagellar
12 length. Linear fit (gray and red lines) and coefficient of determination are indicated. Shading
13 indicates 95% confidence interval.

14

15 Figure 6: Kinesin-13 exponentially and dynamically localizes to the flagellar tip.

16 (A) Representative images and quantification (B) of CRISPRi mediated knockdown of kinesin-13
17 (gRNA+60, red) as compared to a non-specific (ns, gray) gRNA. Blue traces indicate anterior
18 flagella, magenta traces indicate the ventral flagella, green traces indicate the posteriolateral
19 flagella, and orange traces indicate the caudal flagella. (C) Representative image of trophozoites
20 expressing kinesin-13mNG with the cell membrane labeled to indicate the membrane-bound
21 regions of the flagella. Scale bar, 5 μ m. (D) Kinesin-13mNG intensity profiles from the flagellar

1 tip to the base of the membrane-bound regions of caudal (orange), posteriolateral (green), and
2 anterior (blue) flagella. Shading indicates standard error of the mean. $n \geq 23$ for each flagellar
3 pair, from two independent experiments. (E) Mean flagellar tip intensity plotted for each
4 flagellar pair. 95% confidence intervals are indicated. Student's t-test, $*p < 0.05$. (F) Time series
5 images of trophozoites expressing kinesin-13mNG prebleach, immediately post-bleach (0 sec,
6 arrows) of caudal and posteriolateral flagellar tip regions, and during recovery (time in
7 minutes). Scale bar, $2\mu\text{m}$. (G) Time averaged fluorescent recovery of caudal flagellar tip regions
8 following photobleaching. Solid black lines indicate fit of the entire recovery phase and shading
9 indicates the 95% confidence interval. $n = 19$ caudal flagellar tips, from two independent
10 experiments.

11

12 Figure 7: Length-dependent disassembly control flagellar length in *Giardia*.

13 (A) Schematic representation of the "limited precursor" model. The pool of depolymerizing
14 motors does not exchange between different flagella and the pool of depolymerizing motors is
15 greater for shorter flagella than longer flagella at equilibrium. The concentration of
16 depolymerizing motors is also greater at the tip of shorter flagella than longer flagella. (B)
17 Schematic representation of the "excess precursor" model. The pool of depolymerizing motors
18 does not exchange between different flagella and the pool of depolymerizing motors is greater
19 for shorter flagella than longer flagella. The concentration of depolymerizing motors at the
20 flagellar tip is equivalent for short and long flagella at equilibrium. (C, D) The rates of assembly
21 (k^+) and disassembly for short (k^-_{short}) and long (k^-_{long}) flagella as a function of length. (C) The

1 assembly rate (k^+) decreases as a function of length in the “limited precursor” model due to the
2 depletion of the precursor from the pool as flagellar length increases. (D) The assembly rate (k^+)
3 is independent of length in the “excess precursor” model as this model assumes no depletion of
4 the precursor pool. For both models the assembly and disassembly rates are balanced at
5 distinct equilibrium lengths (L_s^* , L_L^*); the balance point also specifies the concentration of
6 kinesin-13 at the tip (C^*). Red lines indicate predicted changes to flagella length (L_s^{taxol} , L_L^{taxol})
7 and flagellar tip concentration of kinesin-13 (C_s^{taxol} , C_L^{taxol}) with Taxol induced elongation of
8 flagella. (E) Representative image of trophozoites expressing kinesin-13mNG and treated with
9 20 μ M Taxol for 1 hour, with the cell membrane labeled to indicate the membrane-bound
10 regions of the flagella. Scale bar, 5 μ m. (F) Flagellar tip intensity of kinesin-13mNG expressing
11 trophozoites treated with DMSO (‘-’) or 20 μ M Taxol (‘+’). $n \geq 12$ cells from two separate
12 experiments were measured for each condition. Means and 95% confidence intervals are
13 indicated.

14

15 Figure 8: *Giardia* utilizes multimodal flagellar assembly and length-dependent disassembly to
16 control four unique flagellar lengths.

17 (A) Schematic of flagellar assembly and maintenance in *Giardia lamblia*. IFT particles move
18 diffusively in the cytoplasmic axoneme regions. IFT trains are assembled in the flagellar pore
19 region and are injected into the membrane-bound region of the axoneme. Within the
20 membrane-bound region, IFT particles undergo anterograde transport via kinesin-2 mediated
21 transport until they reach the distal flagellar tip. IFT trains are reorganized into retrograde

1 directed trains and carried back to the flagellar base by IFT dynein. Kinesin-2 and kinesin-13 are
2 not included in retrograde IFT trains, and instead diffuse back to the flagellar base. While
3 kinesin-2 can freely diffuse to the flagellar base, kinesin-13 can be 'recaptured' by anterograde
4 IFT trains and carried back to the distal tip (Naoz et al., 2008). (B) Predicted fluorescence
5 intensity profiles of the various IFT components in the membrane-bound region of the flagellar
6 axoneme. Bi-directional transport gives a fluorescent signal that does not change with length
7 (IFT-A, IFT-B, IFT dynein). Uni-directional transport coupled with free diffusion is expected to
8 give a profile that decreases linearly from the flagellar tip to the base (Kinesin-2). Uni-
9 directional transport coupled with diffusion and anterograde recapture gives a profile that
10 decreases exponentially from the distal flagellar tip (Kinesin-13) (Naoz et al., 2008). (C) The
11 rates of polymerization (k^+) and depolymerization for short (k^-_{short}) and long (k^-_{long}) flagella as a
12 function of length. The polymerization rate is length-independent, while depolymerization rates
13 are length-dependent. These rates intersect to give two distinct equilibrium lengths (L_{short}^* ,
14 L_{long}^*) with equal concentrations of kinesin-13 at the distal flagellar tip.

15

16 Supplemental Figure 1: Quantification of full axoneme lengths in *Giardia lamblia*.

17 Flagellar length quantification of membrane-bound and cytoplasmic regions of flagellar pairs of
18 *Giardia* trophozoites expressing single-copy, integrated mNeonGreen- β -tubulin. The 95%
19 confidence interval and average length are indicated for cytoplasmic (red) and membrane-
20 bound (blue) regions. $n \geq 35$ flagella for each pair from 3 independent experiments.

21

1 Supplemental Figure 2: PCR validation of IFT81mNG and IFT81GFP integration into the native
2 genomic loci.

3 (A) Schematic representation of primers designed to detect single-copy integration of
4 IFT81mNeonGreen and IFT81GFP constructs. (B) PCR validation of IFT81mNeonGreen and
5 IFT81GFP integration into the native genomic locus. Specific bands are detected for each strain
6 and positive control amplification (CWP1) is detected for all tested strains.

7

8 Supplemental Figure 3: Comparison of brightness between IFT81GFP and IFT81mNG.

9 (A) Representative image of IFT81mNeonGreen and (B) IFT81GFP. Both images are maximum
10 intensity projections acquired with the same acquisition parameters (30ms exposure, 60% laser
11 power).

12

13 Supplemental Figure 4: Kinesin-13mNG flagellar length changes and intensity profiles following
14 flagellar elongation with Taxol.

15 (A) Kinesin-13mNG intensity profiles from the flagellar tip to the base of the membrane-bound
16 regions of caudal (top), posteriolateral (middle), and anterior (bottom) flagella. Orange traces
17 indicate control (DMSO treated) cells and blue traces indicate Taxol treated cells. Shading
18 indicates standard error of the mean. (B) Flagellar length of kinesin-13mNG trophozoites
19 treated with DMSO (opaque) or 20 μ M Taxol (filled). $n \geq 12$ cells from two separate experiments
20 were measured for each condition. Means and 95% confidence intervals are indicated.

1

2 Supplemental Video 1: Fluorescence recovery of IFT81mNG after photobleaching of
3 posteriolateral cytoplasmic axonemes.

4 Fluorescence recovery following photobleaching of the left posteriolateral cytoplasmic
5 axoneme in trophozoites expressing IFT81mNG. The video was recorded at 1 frame/second and
6 is played at 10x increased speed. Time post-bleach (in minutes) is indicated in the top left
7 corner. Scale bar, 5 μ m.

8

9 Supplemental Video 2: Fluorescence recovery of IFT81mNG after photobleaching of anterior
10 and posteriolateral flagellar pores.

11 Fluorescence recovery following photobleaching of the right posteriolateral flagellar pore (top
12 left) and right anterior flagellar pore (bottom right) in trophozoites expressing IFT81mNG. The
13 video was recorded at 1 frame/second and is played at 10x increased speed. Time post-bleach
14 (in minutes) is indicated in the top left corner. Scale bar, 5 μ m.

15

16 Supplemental Video 3: Tracking IFT trains in *Giardia lamblia*.

17 IFT train movement visualized using spinning-disc confocal microscopy in trophozoites
18 expressing IFT81mNG. The video was recorded at ~13 frames/second and is played in real time
19 (indicated in the top left corner, in seconds). Scale bar, 5 μ m.

20

1 Supplemental Video 4: Fluorescence recovery of kinesin-13mNG after photobleaching of caudal
2 and posteriolateral flagellar tips.

3 Fluorescence recovery following photobleaching of the flagellar tips of caudal (left) and
4 posteriolateral (right) flagellar tips in trophozoites expressing kinesin-13mNG. The video was
5 recorded at 1 frame/second and is played at 10x increased speed. Time post-bleach (in
6 minutes) is indicated in the top left corner. Scale bar, 5µm.

7

8 **References**

- 9 Aurrecochea, C., Brestelli, J., Brunk, B. P., Carlton, J. M., Dommer, J., Fischer, S., ... Wang, H.
10 (2009). GiardiaDB and TrichDB: integrated genomic resources for the eukaryotic protist
11 pathogens *Giardia lamblia* and *Trichomonas vaginalis*. *Nucleic Acids Research*, 37(Database
12 issue), D526-30. <https://doi.org/10.1093/nar/gkn631>
- 13 Avidor-Reiss, T., Ha, A., & Basiri, M. L. (2017). Transition Zone Migration: A Mechanism for
14 Cytoplasmic Ciliogenesis and Postaxonemal Centriole Elongation. *Cold Spring Harbor
15 Perspectives in Biology*, 9(8), a028142. <https://doi.org/10.1101/cshperspect.a028142>
- 16 Avidor-Reiss, T., & Leroux, M. R. (2015). Shared and distinct mechanisms of compartmentalized
17 and cytosolic ciliogenesis. *Current Biology*. Elsevier Ltd.
18 <https://doi.org/10.1016/j.cub.2015.11.001>
- 19 Ball, G., Demmerle, J., Kaufmann, R., Davis, I., Dobbie, I. M., & Schermelleh, L. (2015). SIMcheck:
20 a Toolbox for Successful Super-resolution Structured Illumination Microscopy. *Scientific*

- 1 *Reports*, 5, 15915. <https://doi.org/10.1038/srep15915>
- 2 Barker, A. R., Renzaglia, K. S., Fry, K., & Dawe, H. R. (2014). Bioinformatic analysis of ciliary
3 transition zone proteins reveals insights into the evolution of ciliopathy networks. *BMC*
4 *Genomics*, 15(1), 531. <https://doi.org/10.1186/1471-2164-15-531>
- 5 Berman, S. A., Wilson, N. F., Haas, N. A., & Lefebvre, P. A. (2003). A Novel MAP Kinase Regulates
6 Flagellar Length in *Chlamydomonas*. *Current Biology*, 13(13), 1145–1149.
7 [https://doi.org/10.1016/S0960-9822\(03\)00415-9](https://doi.org/10.1016/S0960-9822(03)00415-9)
- 8 Blaineau, C., Tessier, M., Dubessay, P., Tasse, L., Crobu, L., Pagès, M., & Bastien, P. (2007). A
9 Novel Microtubule-Depolymerizing Kinesin Involved in Length Control of a Eukaryotic
10 Flagellum. *Current Biology*, 17(9), 778–782. <https://doi.org/10.1016/j.cub.2007.03.048>
- 11 Bradley, B. A., & Quarmby, L. M. (2005). A NIMA-related kinase, Cnk2p, regulates both flagellar
12 length and cell size in *Chlamydomonas*. *Journal of Cell Science*, 118(Pt 15), 3317–3326.
13 <https://doi.org/10.1242/jcs.02455>
- 14 Brooks, E. R., & Wallingford, J. B. (2014). Multiciliated cells. *Current Biology : CB*, 24(19), R973-
15 82. <https://doi.org/10.1016/j.cub.2014.08.047>
- 16 Buchel, L. A., Gorenflot, A., Chochillon, C., Savel, J., & Gobert, J. G. (1987). In vitro excystation of
17 *Giardia* from humans: a scanning electron microscopy study. *The Journal of Parasitology*,
18 73(3), 487–493. Retrieved from <http://www.ncbi.nlm.nih.gov/pubmed/3598798>
- 19 Buisson, J., Chenouard, N., Lagache, T., Blisnick, T., Olivo-Marin, J.-C., & Bastin, P. (2013).
20 Intraflagellar transport proteins cycle between the flagellum and its base. *Journal of Cell*

- 1 *Science*, 126(Pt 1), 327–338. <https://doi.org/10.1242/jcs.117069>
- 2 Chan, K. Y., & Ersfeld, K. (2010). The role of the Kinesin-13 family protein TbKif13-2 in flagellar
3 length control of *Trypanosoma brucei*. *Molecular and Biochemical Parasitology*, 174(2),
4 137–140. <https://doi.org/10.1016/j.molbiopara.2010.08.001>
- 5 Chien, A., Shih, S. M., Bower, R., Tritschler, D., Porter, M. E., & Yildiz, A. (2017). Dynamics of the
6 IFT machinery at the ciliary tip. *ELife*, 6, e28606. <https://doi.org/10.7554/eLife.28606>
- 7 Cooper, J. A., & Schafer, D. A. (2000). Control of actin assembly and disassembly at filament
8 ends. *Current Opinion in Cell Biology*, 12(1), 97–103. <https://doi.org/10.1016/S0955->
9 0674(99)00062-9
- 10 Coyne, B., & Rosenbaum, J. L. (1970). Flagellar elongation and shortening in *Chlamydomonas*: II.
11 Re-utilization of flagellar proteins. *Journal of Cell Biology*, 47(3), 777–781.
12 <https://doi.org/10.1083/jcb.47.3.777>
- 13 Dawson, S. C., Sagolla, M. S., Mancuso, J. J., Woessner, D. J., House, S. A., Fritz-Laylin, L., &
14 Cande, W. Z. (2007). Kinesin-13 regulates flagellar, interphase, and mitotic microtubule
15 dynamics in *Giardia intestinalis*. *Eukaryotic Cell*, 6(12), 2354–2364.
16 <https://doi.org/10.1128/EC.00128-07>
- 17 Deane, J. A., Cole, D. G., Seeley, E. S., Diener, D. R., & Rosenbaum, J. L. (2001). Localization of
18 intraflagellar transport protein IFT52 identifies basal body transitional fibers as the docking
19 site for IFT particles. *Current Biology*, 11(20), 1586–1590. <https://doi.org/10.1016/S0960->
20 9822(01)00484-5

- 1 Desai, A., Verma, S., Mitchison, T. J., & Walczak, C. E. (1999). Kin I kinesins are microtubule-
2 destabilizing enzymes. *Cell*, *96*(1), 69–78. [https://doi.org/10.1016/S0092-8674\(00\)80960-5](https://doi.org/10.1016/S0092-8674(00)80960-5)
- 3 Ellenberg, J., Siggia, E. D., Moreira, J. E., Smith, C. L., Presley, J. F., Worman, H. J., & Lippincott-
4 Schwartz, J. (1997). Nuclear membrane dynamics and reassembly in living cells: targeting
5 of an inner nuclear membrane protein in interphase and mitosis. *The Journal of Cell*
6 *Biology*, *138*(6), 1193–1206. <https://doi.org/10.1083/JCB.138.6.1193>
- 7 Elmendorf, H. G., Dawson, S. C., & McCaffery, J. M. (2003). The cytoskeleton of *Giardia lamblia*.
8 *International Journal for Parasitology*, *33*(1), 3–28. <https://doi.org/10.1016/S0>
- 9 Engel, B. D., Ludington, W. B., & Marshall, W. F. (2009). Intraflagellar transport particle size
10 scales inversely with flagellar length: Revisiting the balance-point length control model.
11 *Journal of Cell Biology*, *187*(1), 81–89. <https://doi.org/10.1083/jcb.200812084>
- 12 Fai, T. G., Mohapatra, L., Kondev, J., & Amir, A. (2019). Length regulation of multiple flagella
13 that self-assemble from a shared pool of components. *BioRxiv*, 1–29.
14 <https://doi.org/10.1101/436360>
- 15 Gibson, D. G., Young, L., Chuang, R.-Y., Venter, J. C., Hutchison, C. A., & Smith, H. O. (2009).
16 Enzymatic assembly of DNA molecules up to several hundred kilobases. *Nature Methods*,
17 *6*(5), 343–345. <https://doi.org/10.1038/nmeth.1318>
- 18 Gourguechon, S., & Cande, W. Z. (2011). Rapid Tagging and Integration of Genes in *Giardia*
19 *intestinalis*. *Eukaryotic Cell*, *10*(1), 142–145. <https://doi.org/10.1128/EC.00190-10>
- 20 Hagen, K. D., Hirakawa, M. P., House, S. A., Schwartz, C. L., Pham, J. K., Cipriano, M. J., ...

- 1 Dawson, S. C. (2011). Novel structural components of the ventral disc and lateral crest in
2 *Giardia intestinalis*. *PLoS Neglected Tropical Diseases*, 5(12), e1442.
3 <https://doi.org/10.1371/journal.pntd.0001442>
- 4 Hao, L., Scholey, J. M., Lagache, T., Blisnick, T., Olivo-Marin, J.-C., & Bastin, P. (2009).
5 Intraflagellar transport at a glance. *Journal of Cell Science*, 122(Pt 7), 889–892.
6 <https://doi.org/10.1242/jcs.023861>
- 7 Hao, L., Thein, M., Brust-Mascher, I., Civelekoglu-Scholey, G., Lu, Y., Acar, S., ... Scholey, J. M.
8 (2011). Intraflagellar transport delivers tubulin isotypes to sensory cilium middle and distal
9 segments. *Nature Cell Biology*, 13(7), 790–798. <https://doi.org/10.1038/ncb2268>
- 10 Hardin, W. R., Li, R., Xu, J., Shelton, A. M., Alas, G. C. M., Minin, V. N., & Paredez, A. R. (2017).
11 Myosin-independent cytokinesis in *Giardia* utilizes flagella to coordinate force generation
12 and direct membrane trafficking. *Proceedings of the National Academy of Sciences of the*
13 *United States of America*, 114(29), E5854–E5863.
14 <https://doi.org/10.1073/pnas.1705096114>
- 15 Helenius, J., Brouhard, G., Kalaidzidis, Y., Diez, S., & Howard, J. (2006). The depolymerizing
16 kinesin MCAK uses lattice diffusion to rapidly target microtubule ends. *Nature*, 441(7089),
17 115–119. <https://doi.org/10.1038/nature04736>
- 18 Hendel, N. L., Thomson, M., & Marshall, W. F. (2018). Diffusion as a Ruler: Modeling Kinesin
19 Diffusion as a Length Sensor for Intraflagellar Transport. *Biophysical Journal*, 114(3), 663–
20 674. <https://doi.org/10.1016/j.bpj.2017.11.3784>

- 1 Hilton, L. K., Gunawardane, K., Kim, J. W., Schwarz, M. C., & Quarmby, L. M. (2013). The Kinases
2 LF4 and CNK2 Control Ciliary Length by Feedback Regulation of Assembly and Disassembly
3 Rates. *Current Biology*, 23(22), 2208–2214. <https://doi.org/10.1016/J.CUB.2013.09.038>
- 4 Hoeng, J. C., Dawson, S. C., House, S. A., Sagolla, M. S., Pham, J. K., Mancuso, J. J., ... Cande, W.
5 Z. (2008). High-resolution crystal structure and in vivo function of a kinesin-2 homologue in
6 *Giardia intestinalis*. *Molecular Biology of the Cell*, 19(7), 3124–3137.
7 <https://doi.org/10.1091/mbc.E07-11-1156>
- 8 Honnappa, S., Gouveia, S. M., Weisbrich, A., Damberger, F. F., Bhavesh, N. S., Jawhari, H., ...
9 Steinmetz, M. O. (2009). An EB1-Binding Motif Acts as a Microtubule Tip Localization
10 Signal. *Cell*, 138(2), 366–376. <https://doi.org/10.1016/j.cell.2009.04.065>
- 11 Ishikawa, T. (2017). Axoneme Structure from Motile Cilia. *Cold Spring Harbor Perspectives in*
12 *Biology*, 9(1), a028076. <https://doi.org/10.1101/cshperspect.a028076>
- 13 Kozminski, K. G., Johnson, K. A., Forscher, P., & Rosenbaum, J. L. (1993). A motility in the
14 eukaryotic flagellum unrelated to flagellar beating. *Proceedings of the National Academy*
15 *of Sciences of the United States of America*, 90(12), 5519–5523. Retrieved from
16 <http://www.ncbi.nlm.nih.gov/pubmed/8516294>
- 17 Lehtreck, K. F. (2015). IFT-Cargo Interactions and Protein Transport in Cilia. *Trends in*
18 *Biochemical Sciences*, 40(12), 765–778. <https://doi.org/10.1016/j.tibs.2015.09.003>
- 19 Lenaghan, S. C., Davis, C. A., Henson, W. R., Zhang, Z., & Zhang, M. (2011). High-speed
20 microscopic imaging of flagella motility and swimming in *Giardia lamblia* trophozoites.

- 1 *Proceedings of the National Academy of Sciences of the United States of America*, 108(34),
2 E550-8. <https://doi.org/10.1073/pnas.1106904108>
- 3 Li, D., Piao, T., Li, P., Luo, M., Pan, J., Guo, Y., ... Wang, L. (2009). A microtubule depolymerizing
4 kinesin functions during both flagellar disassembly and flagellar assembly in
5 *Chlamydomonas*. *Proceedings of the National Academy of Sciences*, 106(12), 4713–4718.
6 <https://doi.org/10.1073/pnas.0808671106>
- 7 Ludington, W. B., Wemmer, K. a, Lehtreck, K. F., Witman, G. B., & Marshall, W. F. (2013).
8 Avalanche-like behavior in ciliary import. *Proceedings of the National Academy of Sciences*
9 *of the United States of America*, 110(10), 3925–3930.
10 <https://doi.org/10.1073/pnas.1217354110>
- 11 Mangeol, P., Prevo, B., & Peterman, E. J. (2016). KymographClear and KymographDirect: two
12 tools for the automated quantitative analysis of molecular and cellular dynamics using
13 kymographs. *Mol Biol Cell*, 27(12), 1948–1957. <https://doi.org/mbc.E15-06-0404>
14 [pii]\r10.1091/mbc.E15-06-0404
- 15 Manning, G., Reiner, D. S., Lauwaet, T., Dacre, M., Smith, A., Zhai, Y., ... Gillin, F. D. (2011). The
16 minimal kinome of *Giardia lamblia* illuminates early kinase evolution and unique parasite
17 biology. *Genome Biology*, 12(7), R66. <https://doi.org/10.1186/gb-2011-12-7-r66>
- 18 Marshall, W. F., Qin, H., Rodrigo Brenni, M., Rosenbaum, J. L., Brenni, M. R., & Rosenbaum, J. L.
19 (2005). Flagellar length control system: testing a simple model based on intraflagellar
20 transport and turnover. *Molecular Biology of the Cell*, 16(1), 270–278.
21 <https://doi.org/10.1091/mbc.E04-07-0586>

- 1 Marshall, W. F., & Rosenbaum, J. L. (1999). Intraflagellar transport balances continuous
2 turnover of outer doublet microtubules : implications for flagellar length control. *The*
3 *Journal of Cell Biology*, 155(3), 405–414. <https://doi.org/10.1083/jcb.200106141>
- 4 McInally, S. G., Hagen, K. D., Nosala, C., Williams, J., Nguyen, K., Booker, J., ... Dawson, S. C.
5 (2019). Robust and stable transcriptional repression in *Giardia* using CRISPRi. *Molecular*
6 *Biology of the Cell*, 30(1), 119–130. <https://doi.org/10.1091/mbc.E18-09-0605>
- 7 McInally, Shane G., & Dawson, S. C. (2016). Eight unique basal bodies in the multi-flagellated
8 diplomonad *Giardia lamblia*. *Cilia*, 5(1), 21. <https://doi.org/10.1186/s13630-016-0042-4>
- 9 Meng, D., & Pan, J. (2016). A NIMA-related kinase, CNK4, regulates ciliary stability and length.
10 *Molecular Biology of the Cell*, 27(5), 838–847. <https://doi.org/10.1091/mbc.E15-10-0707>
- 11 Mohapatra, L., Goode, B. L., Jelenkovic, P., Phillips, R., & Kondev, J. (2016). Design Principles of
12 Length Control of Cytoskeletal Structures. *Annual Review of Biophysics*, 45(1), 85–116.
13 <https://doi.org/10.1146/annurev-biophys-070915-094206>
- 14 Naoz, M., Manor, U., Sakaguchi, H., Kachar, B., & Gov, N. S. (2008). Protein localization by actin
15 treadmilling and molecular motors regulates stereocilia shape and treadmilling rate.
16 *Biophysical Journal*, 95(12), 5706–5718. <https://doi.org/10.1529/biophysj.108.143453>
- 17 Nohynková, E., Tumová, P., & Kulda, J. (2006). Cell division of *Giardia intestinalis*: flagellar
18 developmental cycle involves transformation and exchange of flagella between mastigonts
19 of a diplomonad cell. *Eukaryotic Cell*, 5(4), 753–761. [https://doi.org/10.1128/EC.5.4.753-](https://doi.org/10.1128/EC.5.4.753-761.2006)
20 761.2006

- 1 Pazour, G. J., Dickert, B. L., & Witman, G. B. (1999). The DHC1B (DHC2) isoform of cytoplasmic
2 dynein is necessary for flagellar maintenance as well as flagellar assembly. *Journal of Cell*
3 *Biology*, 144(3), 10--369. Retrieved from
4 <http://citeseerx.ist.psu.edu/viewdoc/summary?doi=10.1.1.273.7263>
- 5 Pazour, G. J., & Witman, G. B. (2003). The vertebrate primary cilium is a sensory organelle.
6 *Current Opinion in Cell Biology*, 15(1), 105–110. [https://doi.org/10.1016/S0955-](https://doi.org/10.1016/S0955-0674(02)00012-1)
7 [0674\(02\)00012-1](https://doi.org/10.1016/S0955-0674(02)00012-1)
- 8 Prevo, B., Mangeol, P., Oswald, F., Scholey, J. M., & Peterman, E. J. G. (2015). Functional
9 differentiation of cooperating kinesin-2 motors orchestrates cargo import and transport in
10 *C. elegans* cilia. *Nature Cell Biology*, 17(12), 1536–1545. <https://doi.org/10.1038/ncb3263>
- 11 Reiter, J. F., Blacque, O. E., & Leroux, M. R. (2012). The base of the cilium: roles for transition
12 fibres and the transition zone in ciliary formation, maintenance and compartmentalization.
13 *EMBO Reports*, 13(7), 608–618. <https://doi.org/10.1038/embor.2012.73>
- 14 Sagolla, M. S., Dawson, S. C., Mancuso, J. J., & Cande, W. Z. (2006). Three-dimensional analysis
15 of mitosis and cytokinesis in the binucleate parasite *Giardia intestinalis*. *Journal of Cell*
16 *Science*, 119(Pt 23), 4889–4900. <https://doi.org/10.1242/jcs.03276>
- 17 Schindelin, J., Arganda-Carreras, I., Frise, E., Kaynig, V., Longair, M., Pietzsch, T., ... Cardona, A.
18 (2012). Fiji: an open-source platform for biological-image analysis. *Nature Methods*, 9(7),
19 676–682. <https://doi.org/10.1038/nmeth.2019>
- 20 Shaner, N. C., Lambert, G. G., Chammas, A., Ni, Y., Cranfill, P. J., Baird, M. A., ... Wang, J. (2013).

- 1 A bright monomeric green fluorescent protein derived from *Branchiostoma lanceolatum*.
2 *Nature Methods*, 10(5), 407–409. <https://doi.org/10.1038/nmeth.2413>
- 3 Sung, C. H., & Leroux, M. R. (2013). The roles of evolutionarily conserved functional modules in
4 cilia-related trafficking. *Nature Cell Biology*, 15(12), 1387–1397.
5 <https://doi.org/10.1038/ncb2888>
- 6 Tamm, S. L. (1967). Flagellar Development in the Protozoan *Peranema trichophorum*. *Journal of*
7 *Experimental Zoology*, 164(2), 163–186. <https://doi.org/10.1002/jez.1401640204>
- 8 Vasudevan, K. K., Jiang, Y.-Y., Lehtreck, K. F., Kushida, Y., Alford, L. M., Sale, W. S., ... Gaertig, J.
9 (2015). Kinesin-13 regulates the quantity and quality of tubulin inside cilia. *Molecular*
10 *Biology of the Cell*, 26(3), 478–494. <https://doi.org/10.1091/mbc.E14-09-1354>
- 11 Walczak, C. E., Gayek, S., Ohi, R., & Wordeman, L. (2013). Microtubule-Depolymerizing Kinesins.
12 *Annual Review of Cell and Developmental Biology*, 29(1), 417–441.
13 <https://doi.org/10.1146/annurev-cellbio-101512-122345>
- 14 Wang, L., Piao, T., Cao, M., Qin, T., Huang, L., Deng, H., ... Pan, J. (2013). Flagellar regeneration
15 requires cytoplasmic microtubule depolymerization and kinesin-13. *Journal of Cell Science*,
16 126(6), 1531–1540. <https://doi.org/10.1242/jcs.124255>
- 17 Wingfield, J. L., Mengoni, I., Bomberger, H., Jiang, Y.-Y., Walsh, J. D., Brown, J. M., ... Lehtreck,
18 K. (2017). IFT trains in different stages of assembly queue at the ciliary base for
19 consecutive release into the cilium. *ELife*, 6. <https://doi.org/10.7554/eLife.26609>
- 20 Wloga, D., Camba, A., Rogowski, K., Manning, G., Jerka-Dziadosz, M., & Gaertig, J. (2006).

1 Members of the NIMA-related kinase family promote disassembly of cilia by multiple
2 mechanisms. *Molecular Biology of the Cell*, 17(6), 2799–2810.
3 <https://doi.org/10.1091/mbc.E05-05-0450>

4 Woessner, D. J., & Dawson, S. C. (2012). The giardia median body protein is a ventral disc
5 protein that is critical for maintaining a domed disc conformation during attachment.
6 *Eukaryotic Cell*, 11(3), 292–301. <https://doi.org/10.1128/EC.05262-11>

7 Wren, K. N. N., Craft, J. M. M., Tritschler, D., Schauer, A., Patel, D. K. K., Smith, E. F. F., ...
8 Lehtreck, K. F. F. (2013). A differential cargo-loading model of ciliary length regulation by
9 IFT. *Current Biology*, 23(24), 2463–2471. <https://doi.org/10.1016/j.cub.2013.10.044>

10

Figure 1

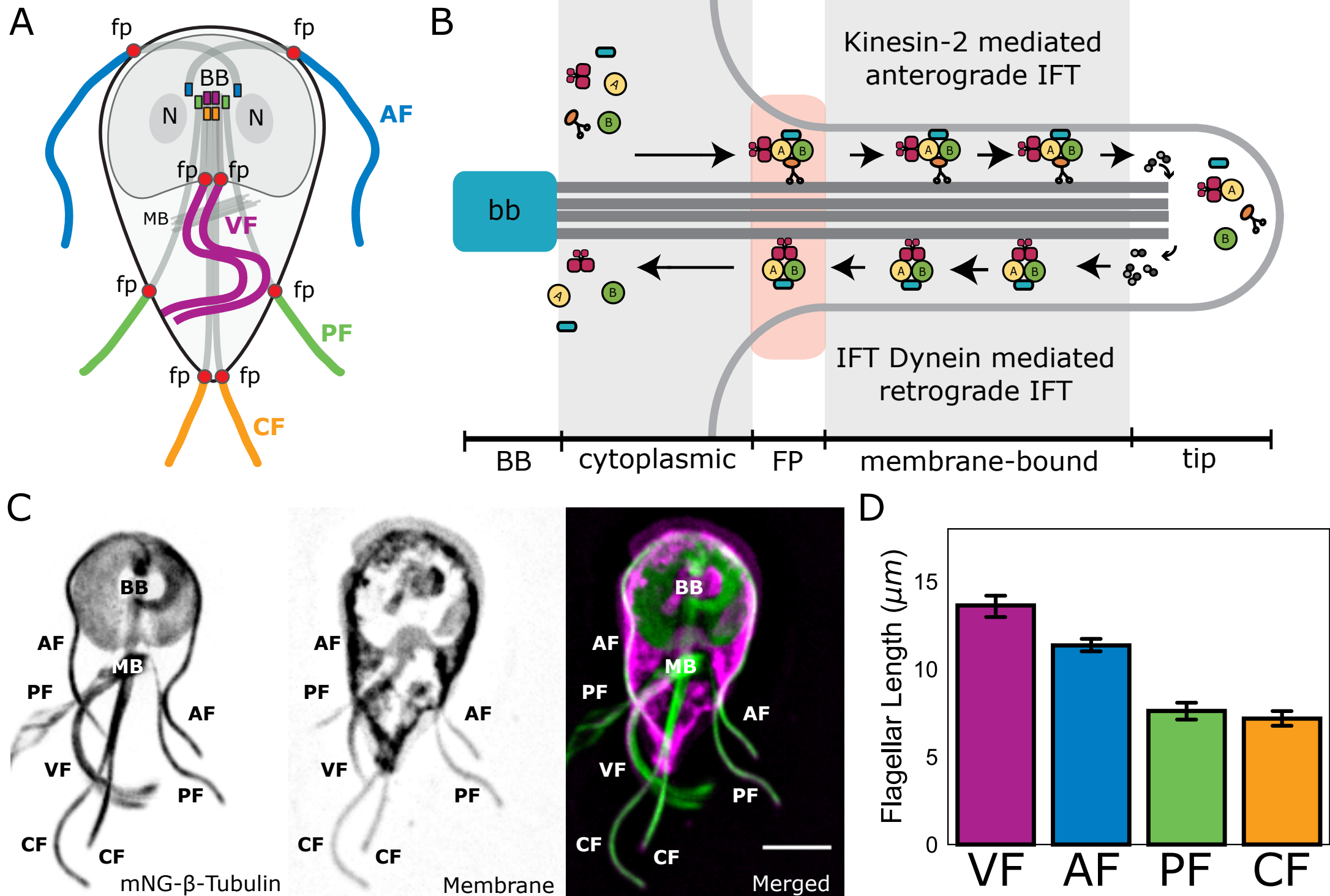


Figure 2

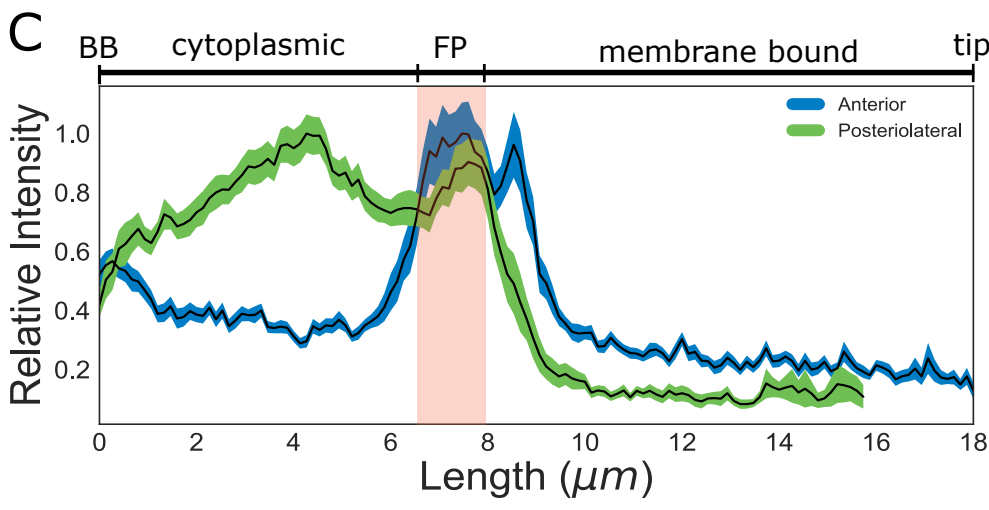
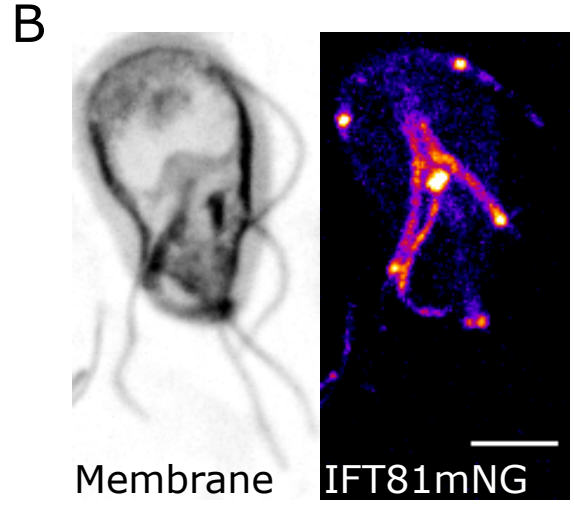
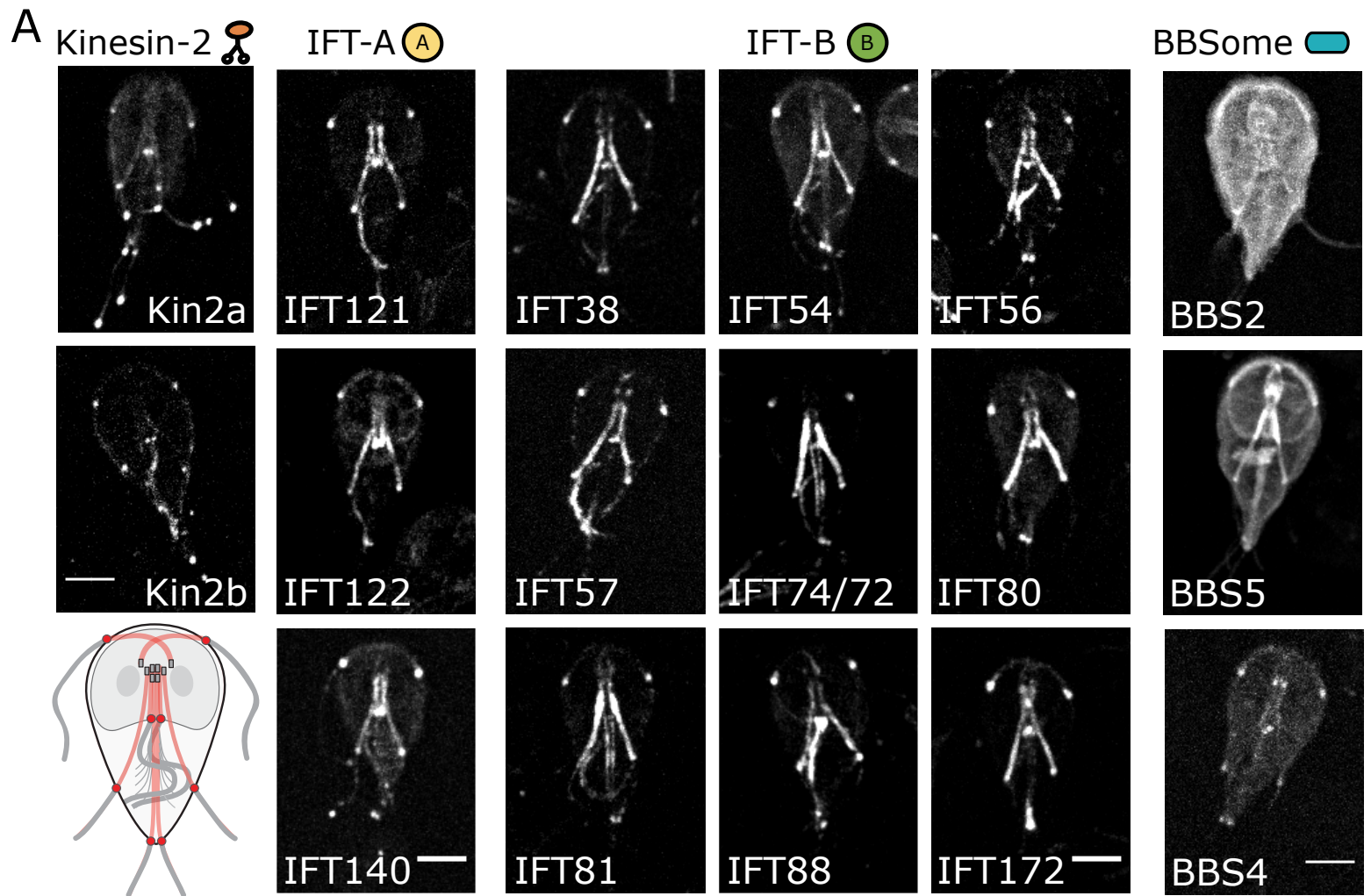


Figure 3

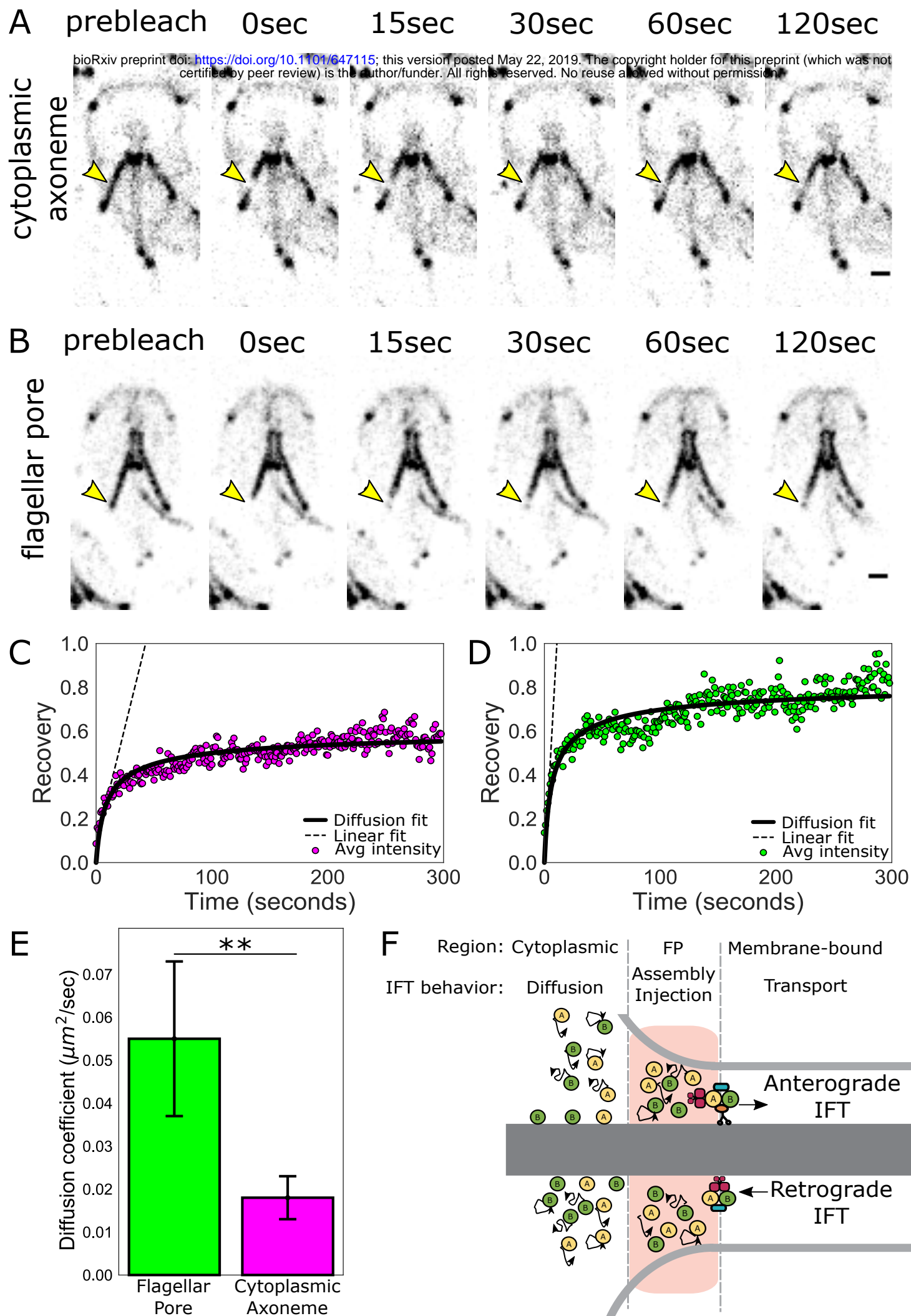
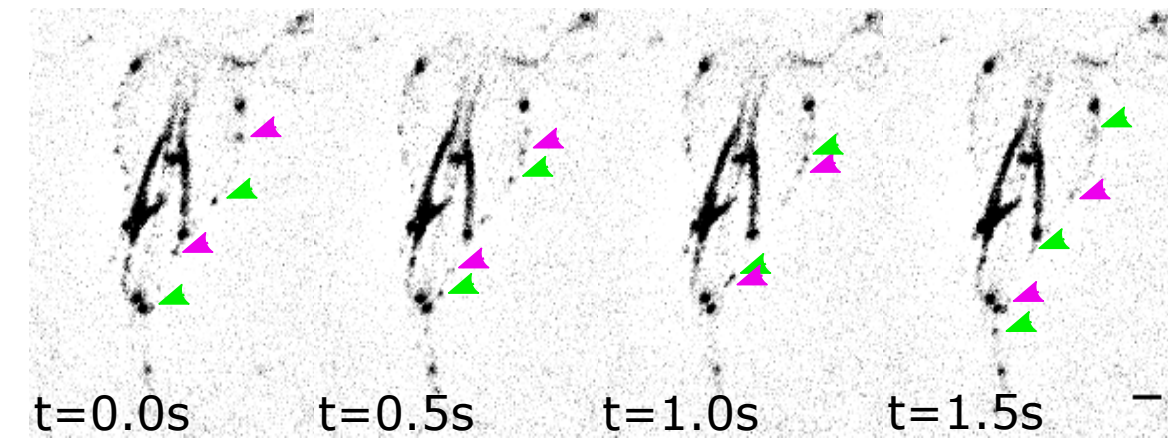
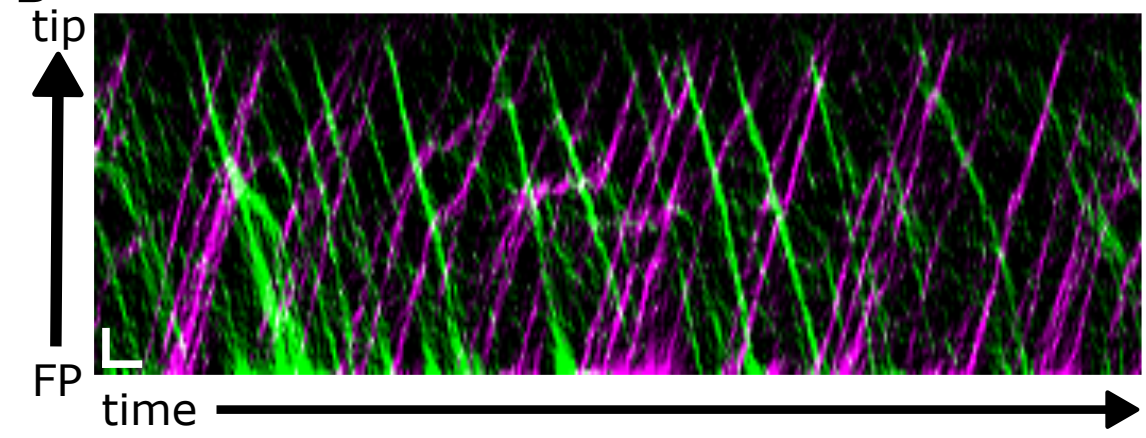


Figure 4

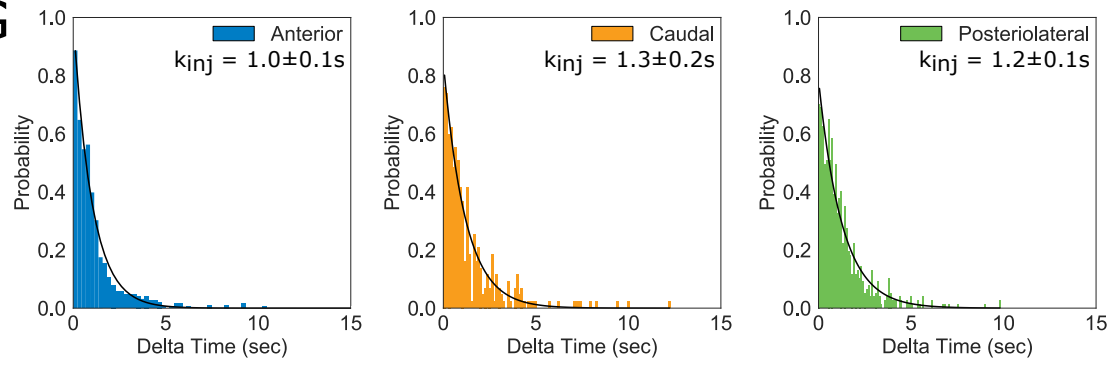
A



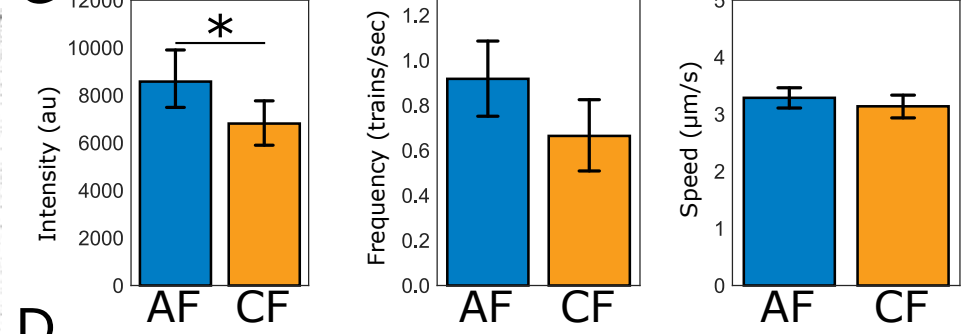
B



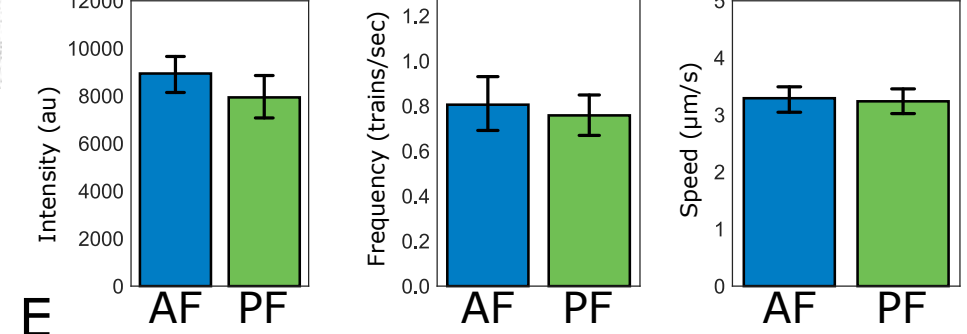
G



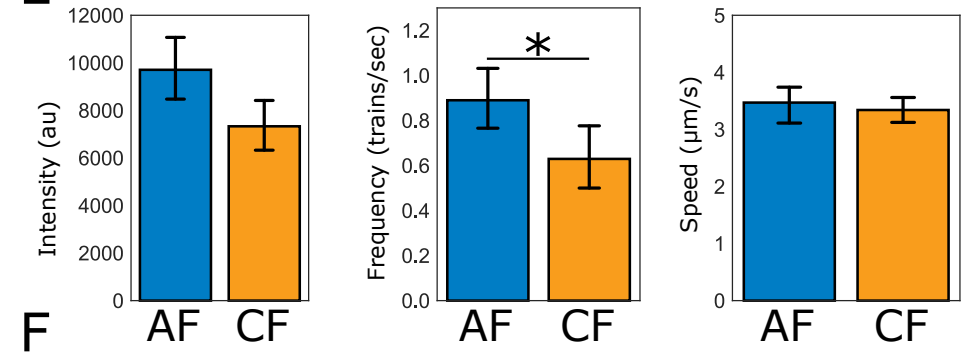
C



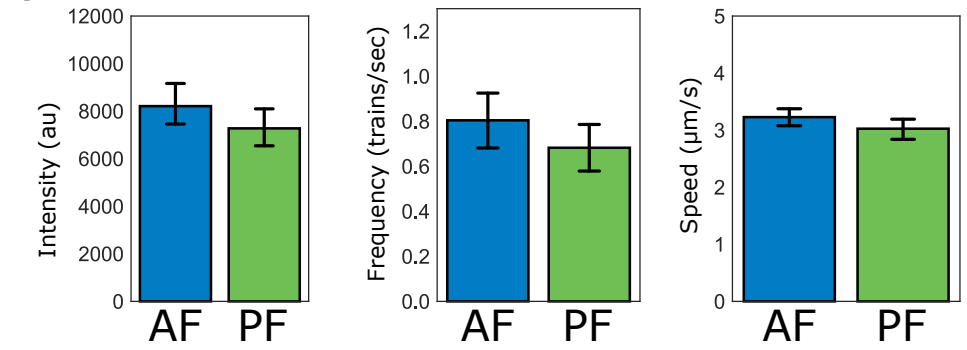
D



E



F



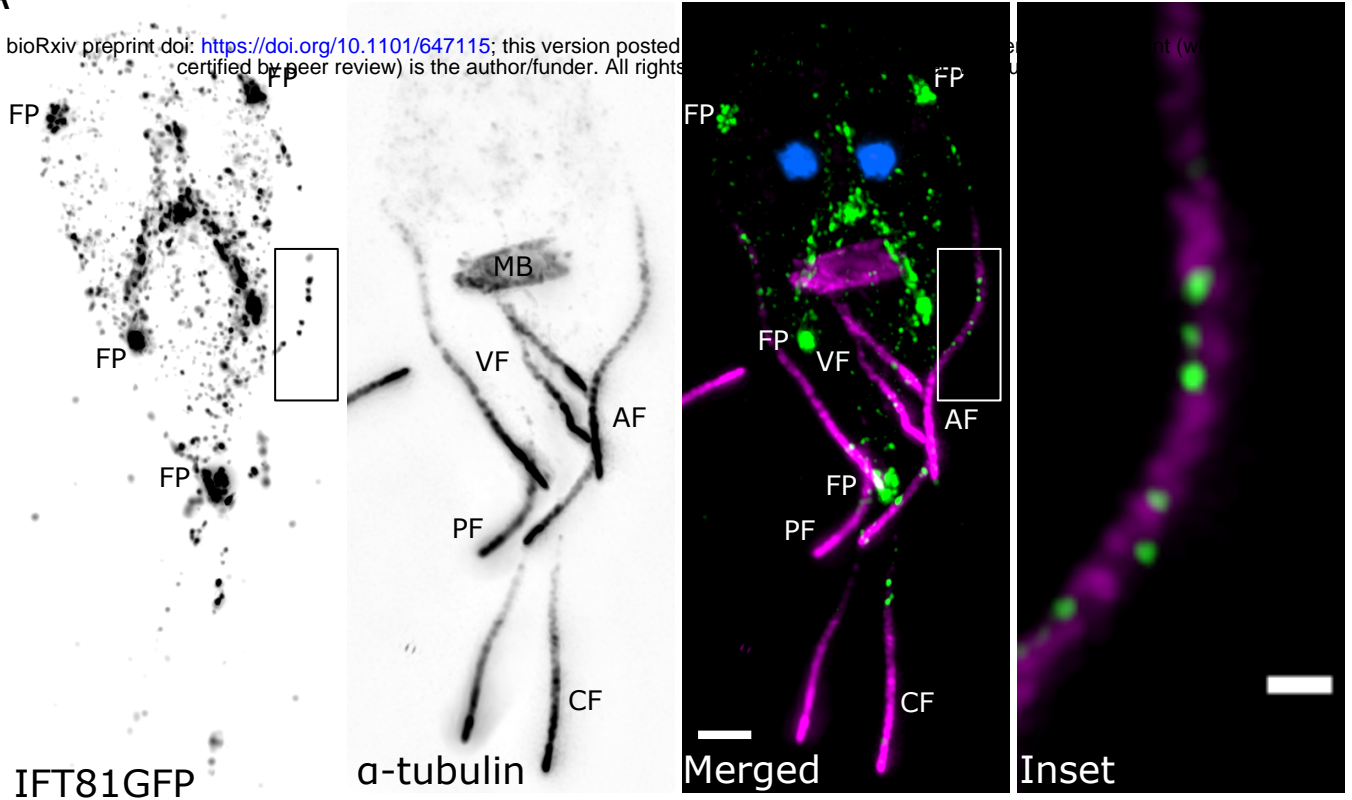
Anterograde

Retrograde

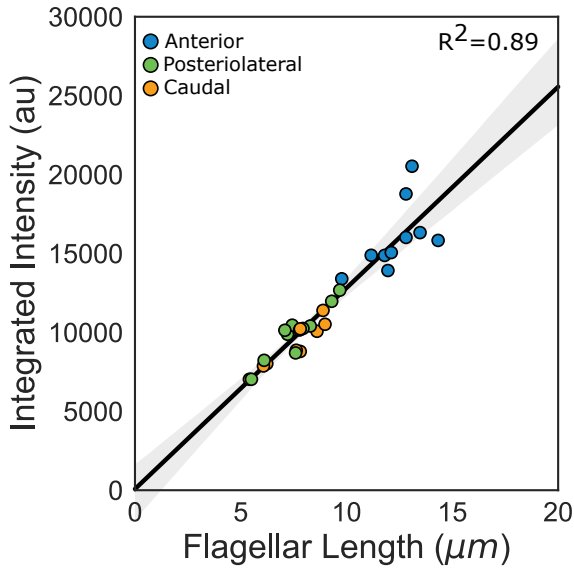
Figure 5

A

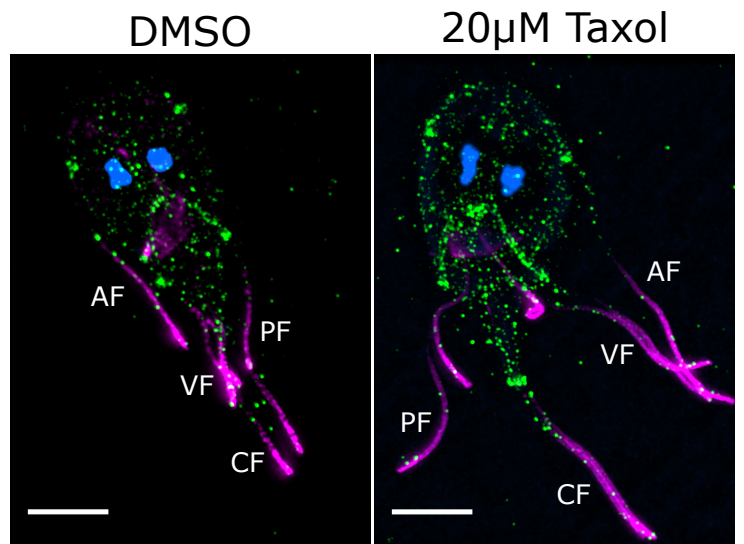
bioRxiv preprint doi: <https://doi.org/10.1101/647115>; this version posted [unclear] (with peer review) is the author/funder. All rights reserved. No reuse allowed without permission.



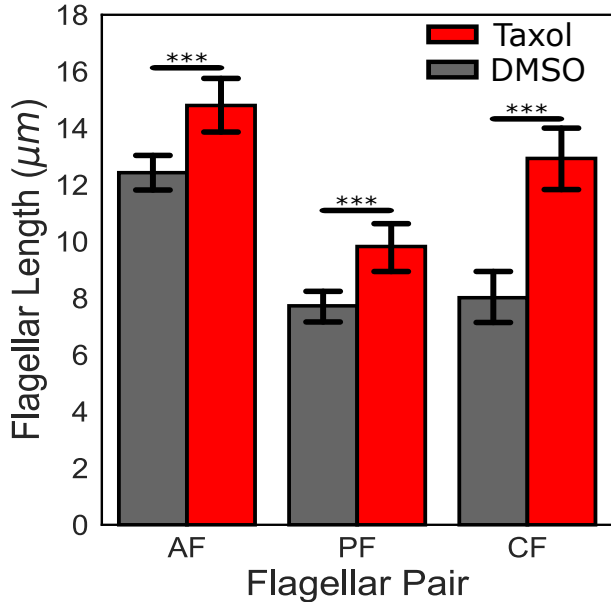
B



C



D



E

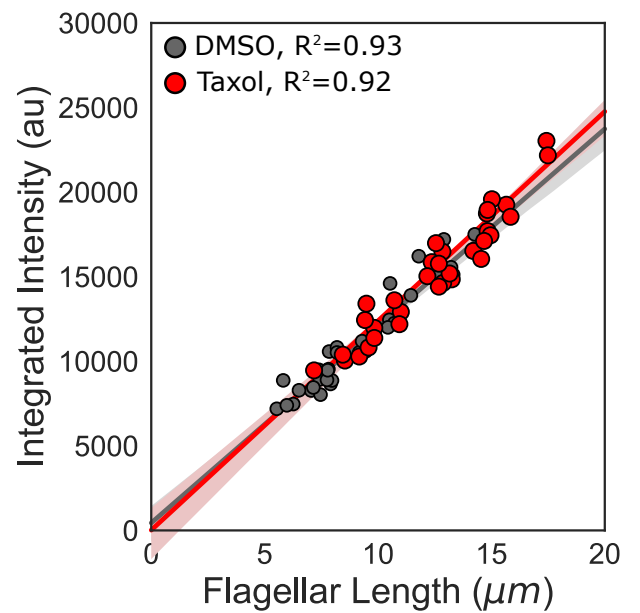


Figure 6

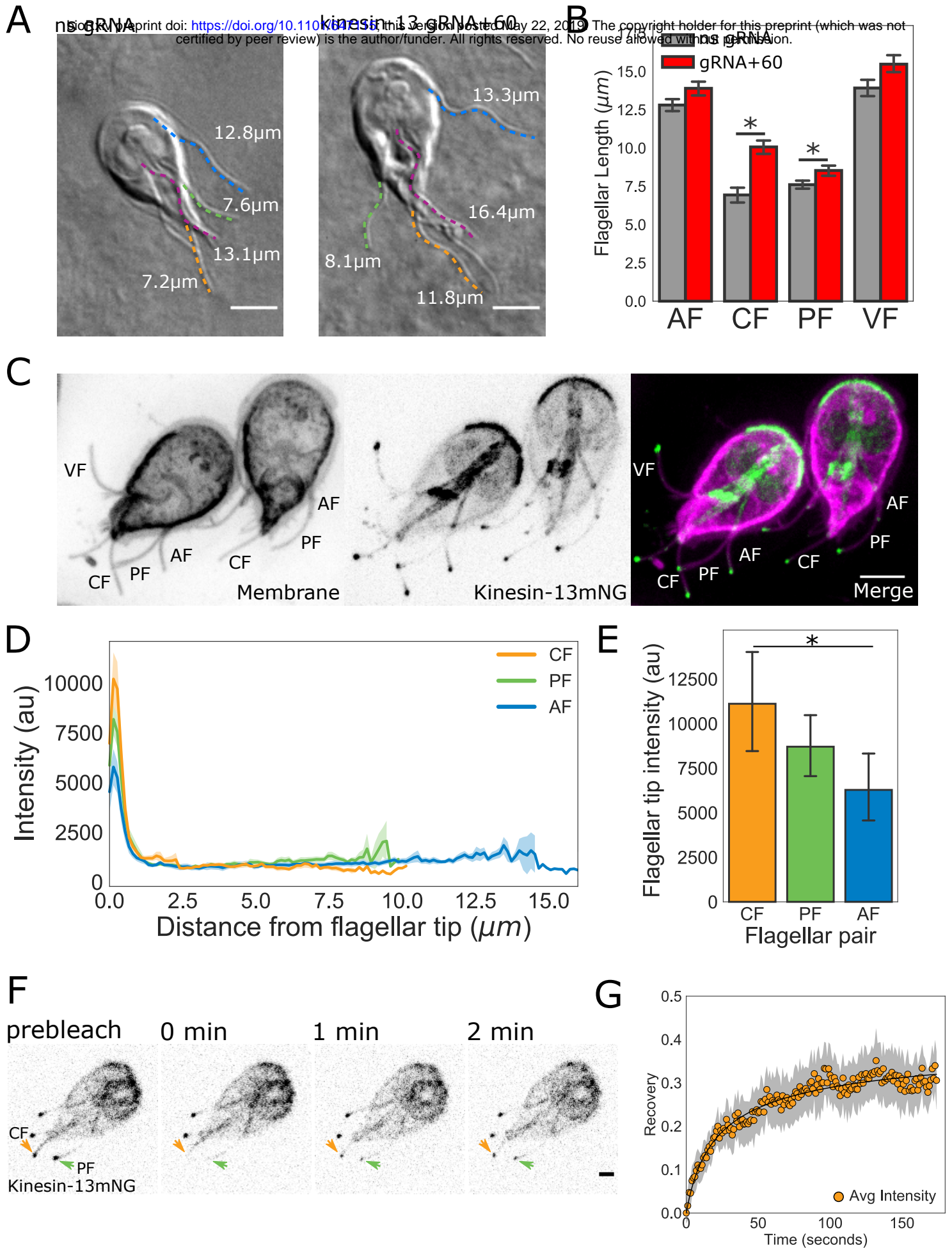


Figure 7

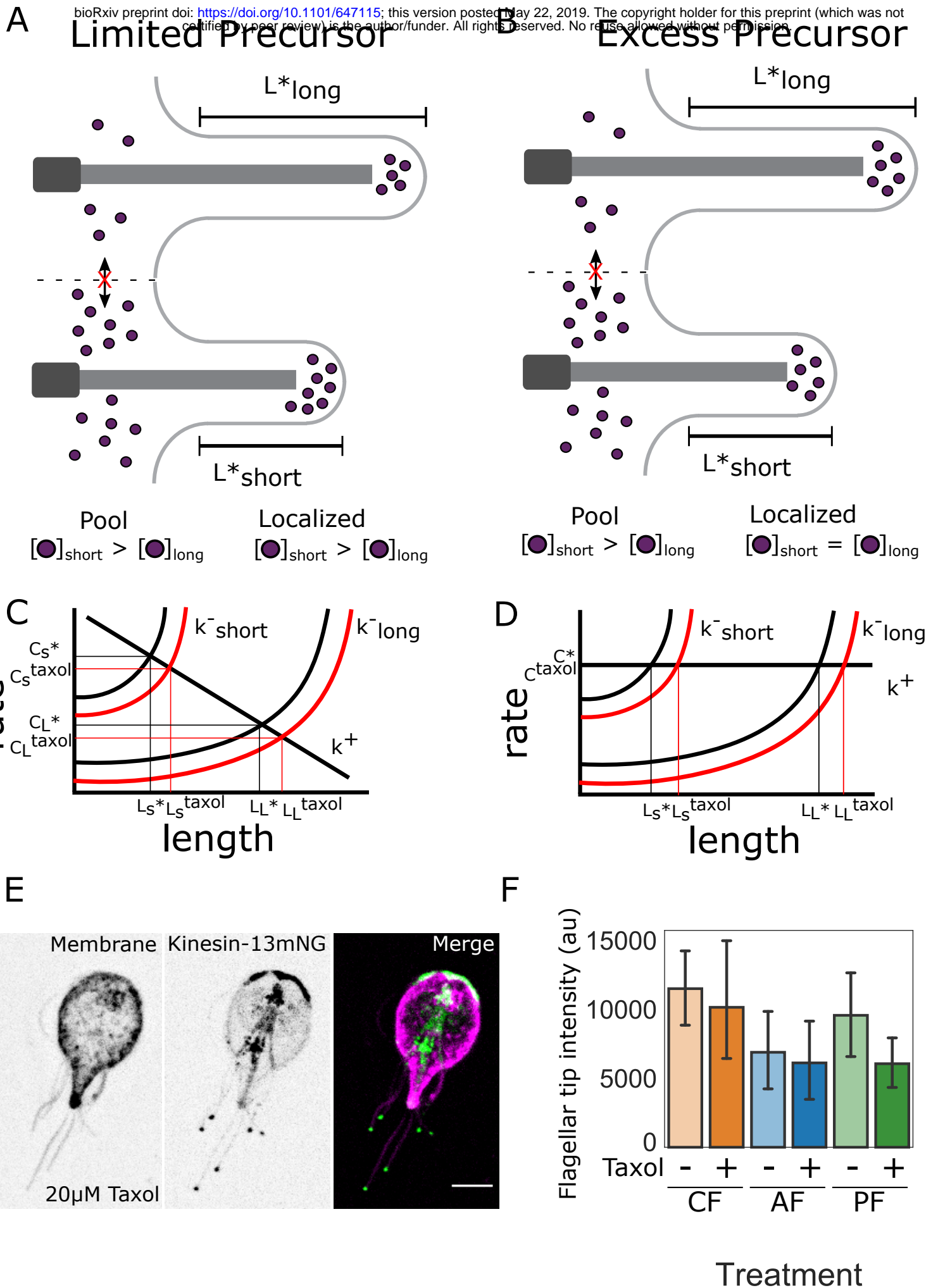
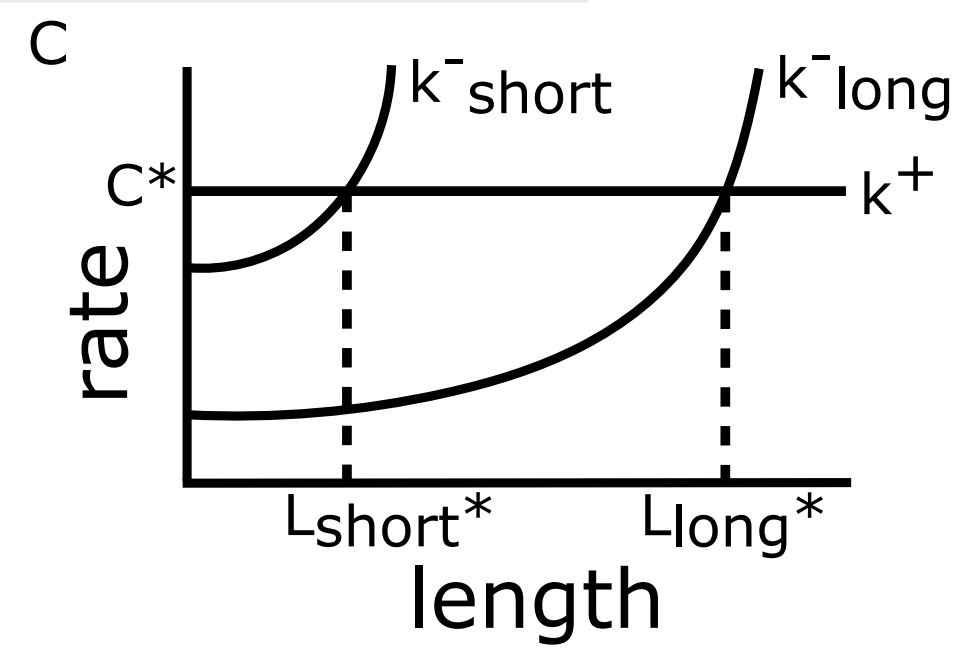
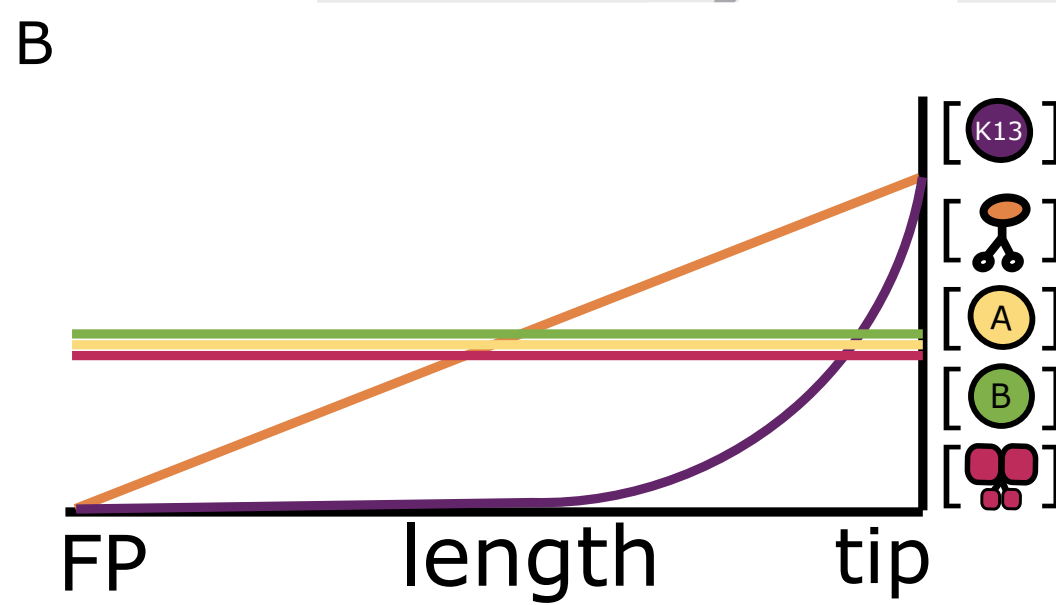
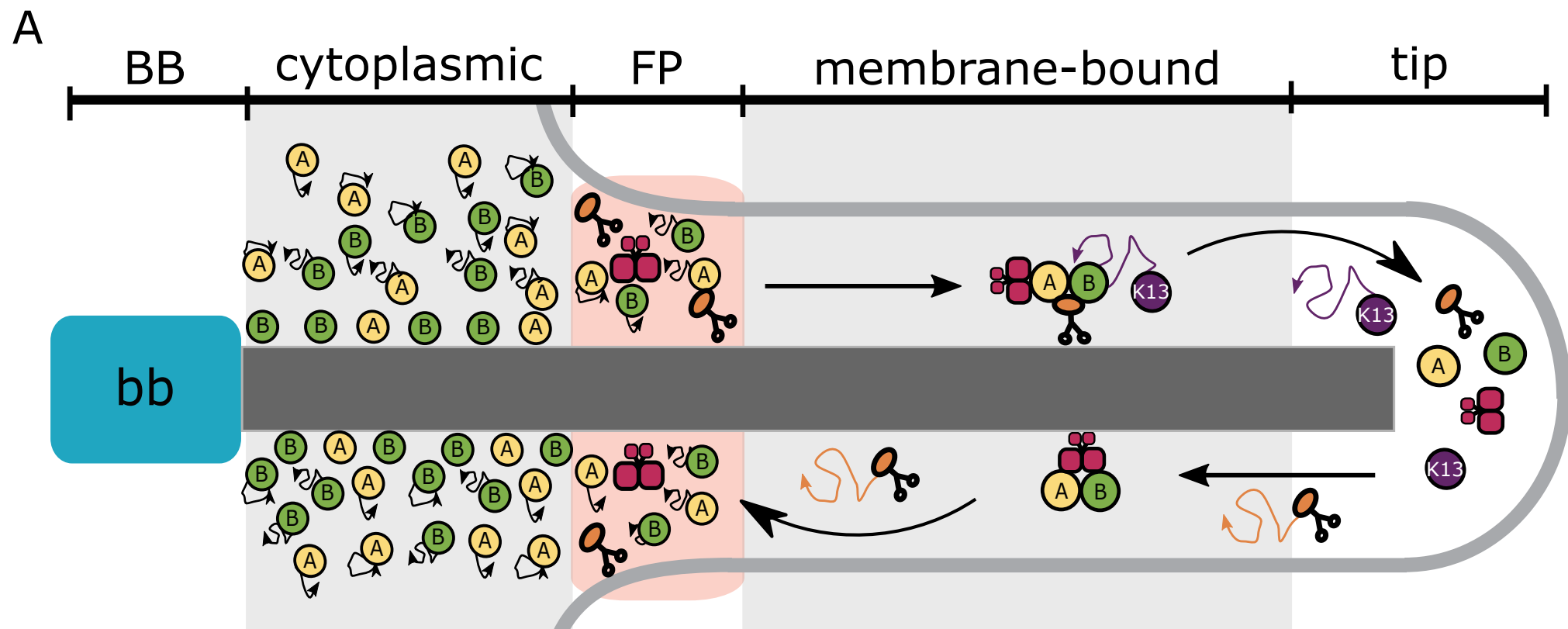
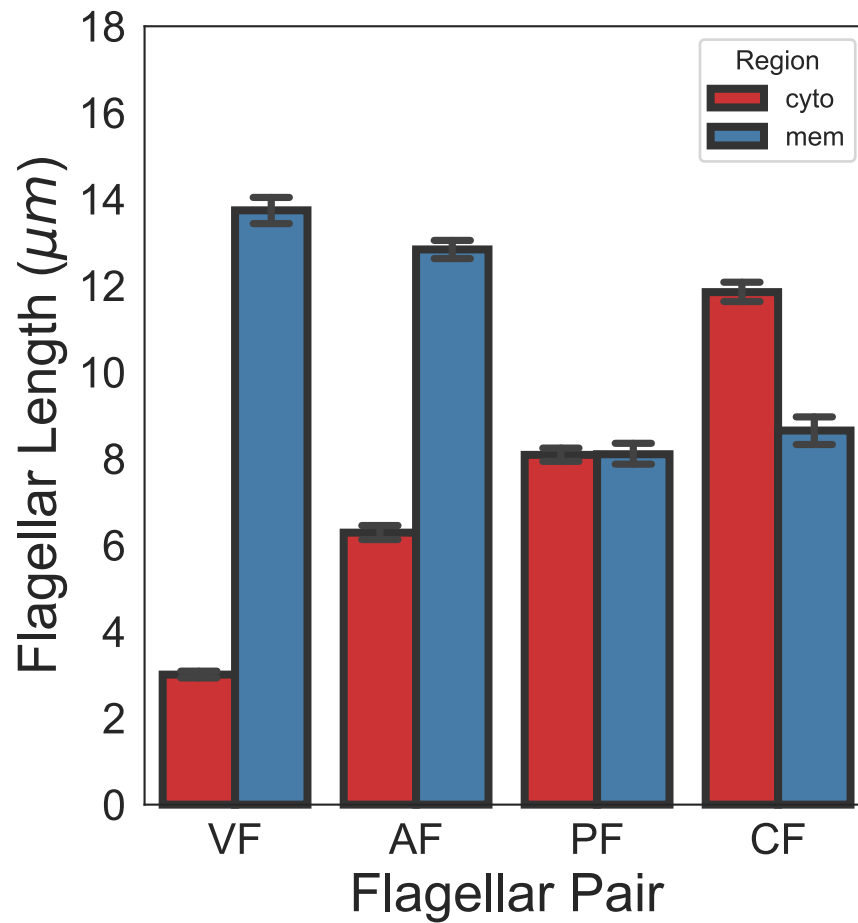


Figure 8



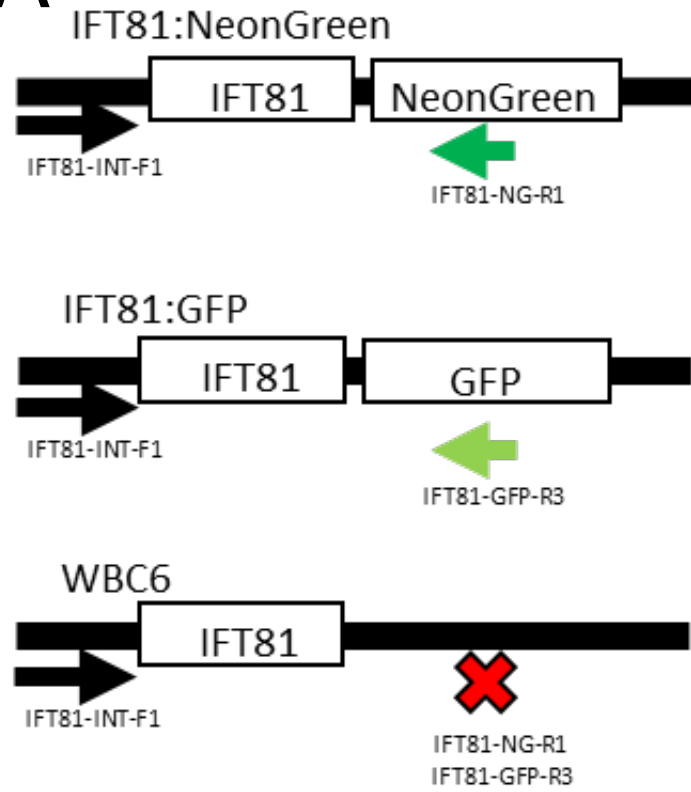
Supplemental figure 1

bioRxiv preprint doi: <https://doi.org/10.1101/647115>; this version posted May 22, 2019. The copyright holder for this preprint (which was not certified by peer review) is the author/funder. All rights reserved. No reuse allowed without permission.

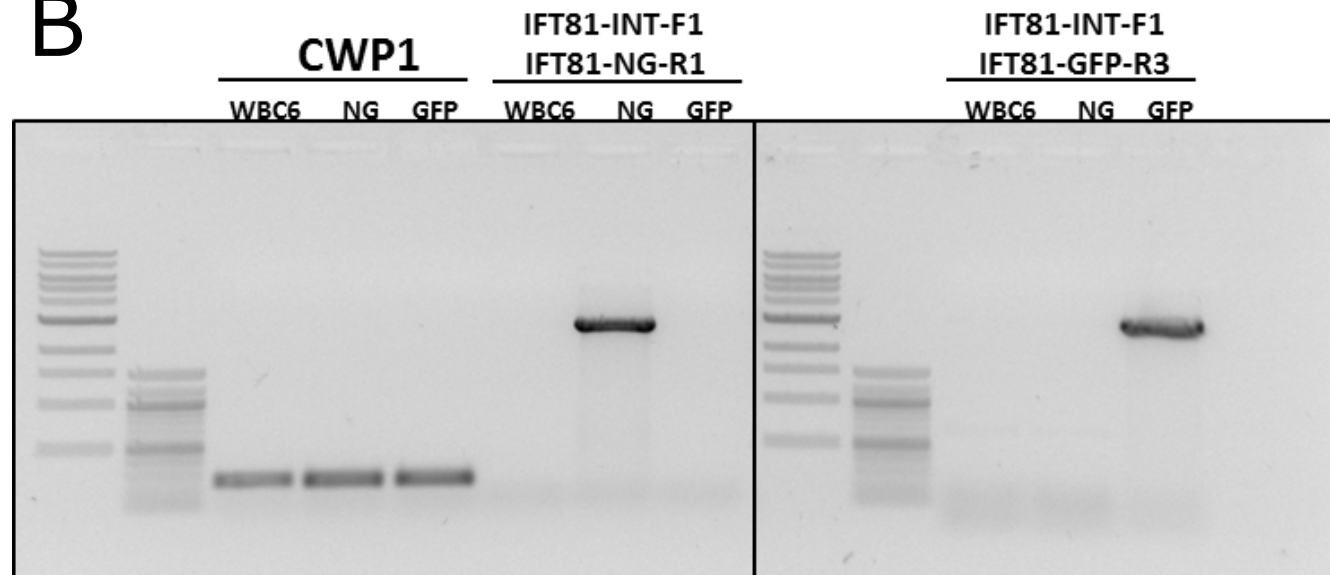


Supplemental figure 2

A

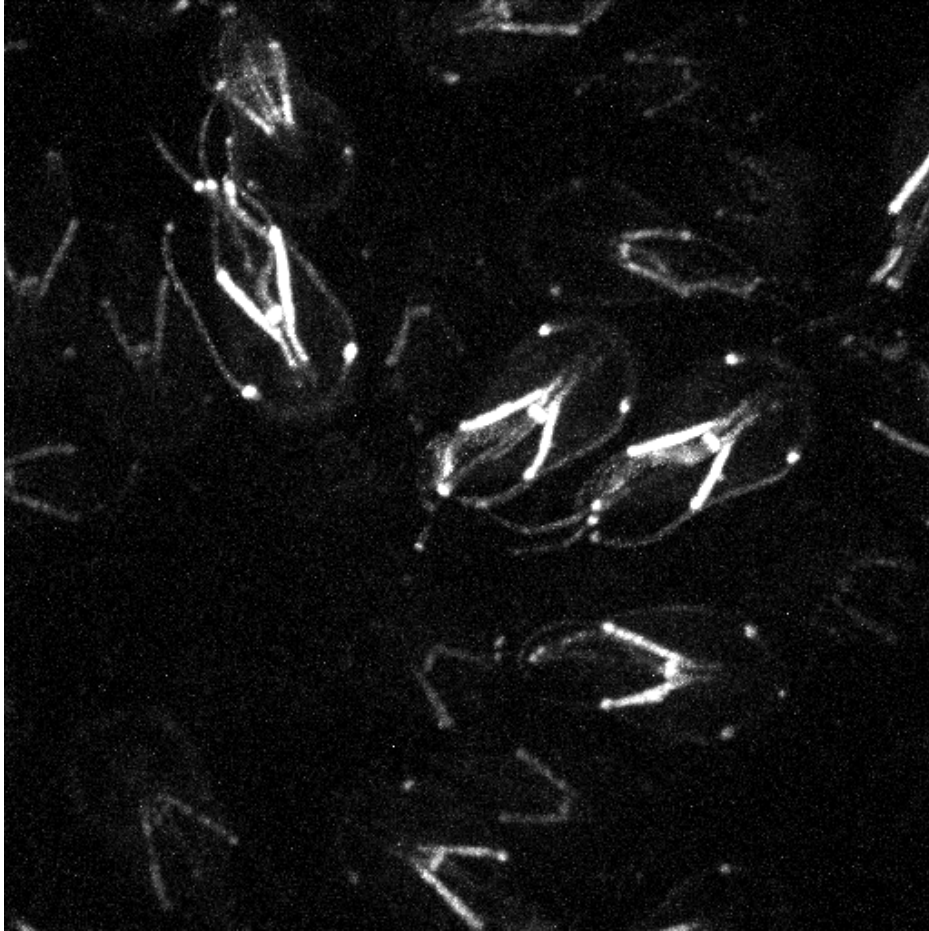


B

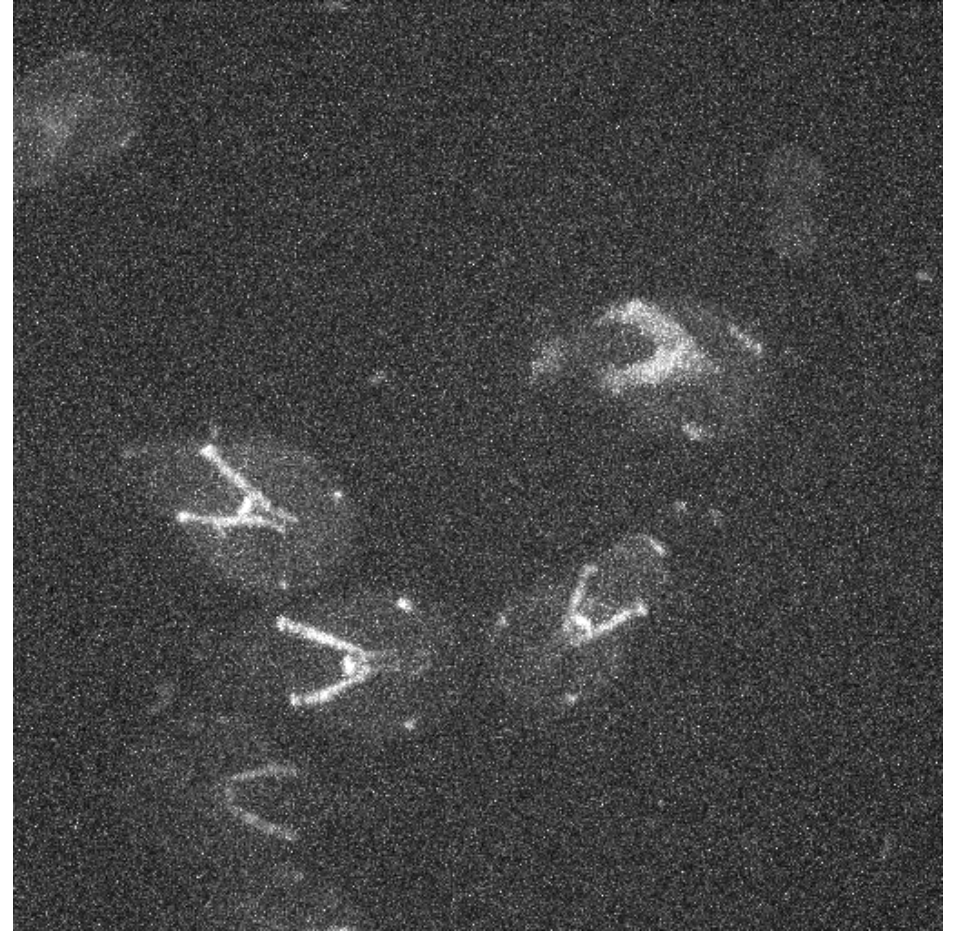


Supplemental figure 3

A IFT81mNeonGreen



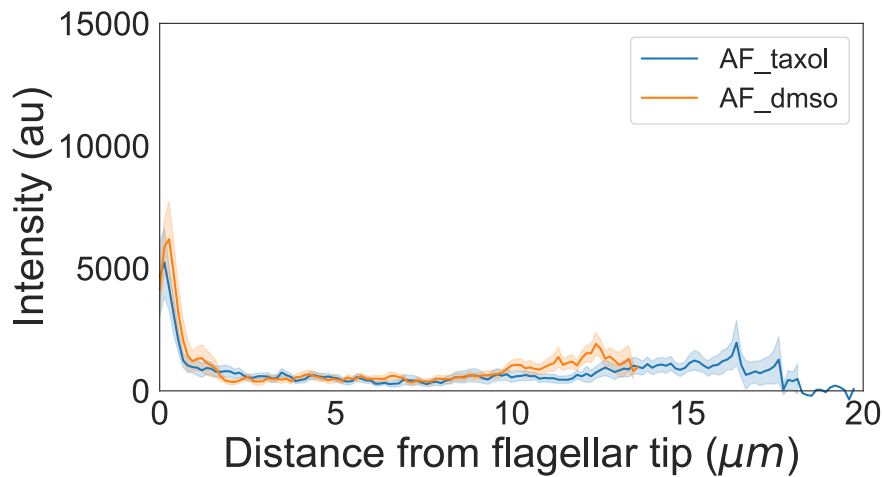
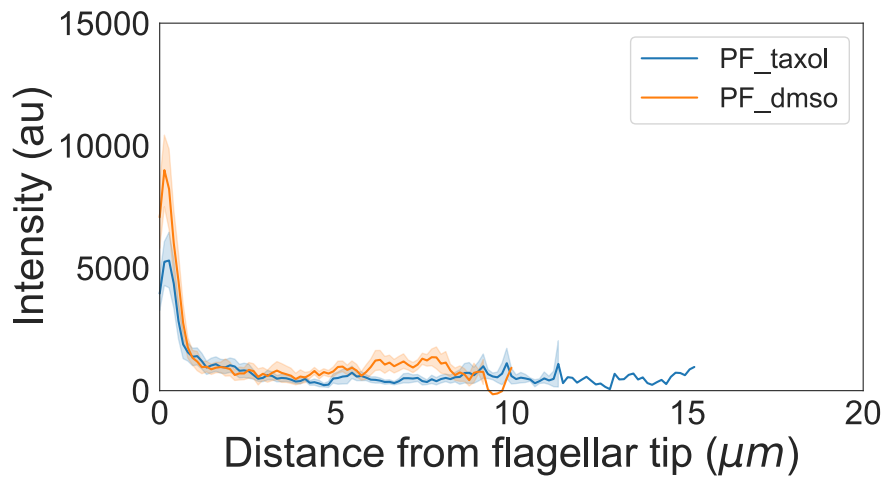
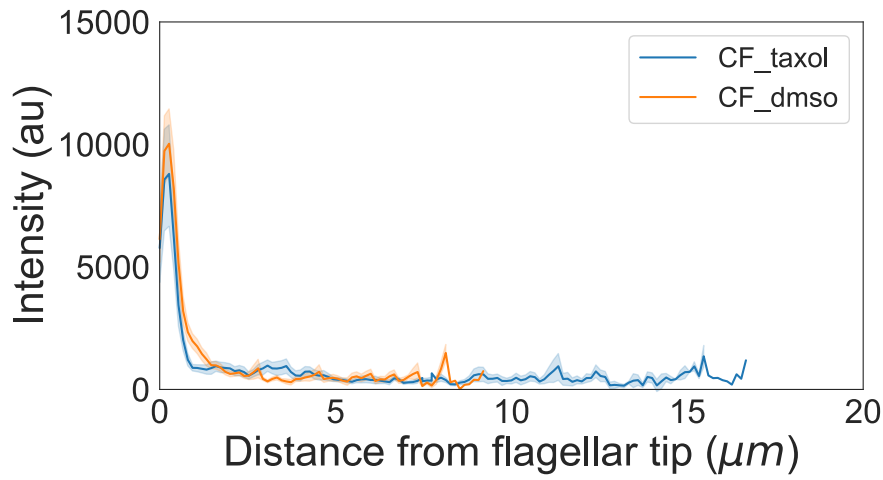
B IFT81GFP



Supplemental figure 4

bioRxiv preprint doi: <https://doi.org/10.1101/647115>; this version posted May 22, 2019. The copyright holder for this preprint (which was not certified by peer review) is the author/funder. All rights reserved. No reuse allowed without permission.

A



B

